DNA 5058F

COMPRESSION AND SHEAR WAVE PROPAGATION IN SALT AND GRANITE

Y. M. Gupta
E. Privitzer
SRI International
333 Ravenswood Avenue
Menlo Park, California 94025

1 August 1979

Final Report for Period 1 June 1978– 1 June 1979

CONTRACT No. DNA 001-76-C-0384

APPROVED FOR PUBLIC RELEASE;
DISTRIBUTION UNLIMITED.

THIS WORK SPONSORED BY THE DEFENSE NUCLEAR AGENCY
UNDER RDT&E RMSS CODE B344077464 Y99QAXSB14414 H2590D.

Prepared for
Director
DEFENSE NUCLEAR AGENCY
Washington, D. C. 20305

Destroy this report when it is no longer needed. Do not return to sender.

PLEASE NOTIFY THE DEFENSE NUCLEAR AGENCY, ATTN: STTI, WASHINGTON, D.C. 20305, IF YOUR ADDRESS IS INCORRECT, IF YOU WISH TO BE DELETED FROM THE DISTRIBUTION LIST, OR IF THE ADDRESSEE IS NO LONGER EMPLOYED BY YOUR ORGANIZATION.

DNA PRINTING PLANT

UNCLASSIFIED

SECURITY CLASSIFICATION OF THIS PAGE *(When Data Entered)*

REPORT DOCUMENTATION PAGE

READ INSTRUCTIONS BEFORE COMPLETING FORM

1. REPORT NUMBER: DNA 5058F	2. GOVT ACCESSION NO.: AD-A090570
3. RECIPIENT'S CATALOG NUMBER:	
4. TITLE *(and Subtitle)*: COMPRESSION AND SHEAR WAVE PROPAGATION IN SALT AND GRANITE	5. TYPE OF REPORT & PERIOD COVERED: Final Report for Period 1 June 1978 - 1 June 1979
	6. PERFORMING ORG. REPORT NUMBER: PYU-5746
7. AUTHOR(s): Y. M. Gupta and E. Privitzer	8. CONTRACT OR GRANT NUMBER(s): DNA 001-76-C-0384
9. PERFORMING ORGANIZATION NAME AND ADDRESS: SRI International, 333 Ravenswood Avenue, Menlo Park, California 94025	10. PROGRAM ELEMENT, PROJECT, TASK AREA & WORK UNIT NUMBERS: Subtask Y99QAXSB144-14
11. CONTROLLING OFFICE NAME AND ADDRESS: Director, Defense Nuclear Agency, Washington, DC 20305	12. REPORT DATE: 1 August 1979
	13. NUMBER OF PAGES: 108
14. MONITORING AGENCY NAME & ADDRESS *(if different from Controlling Office)*	15. SECURITY CLASS *(of this report)*: UNCLASSIFIED
	15a. DECLASSIFICATION/DOWNGRADING SCHEDULE

16. DISTRIBUTION STATEMENT *(of this Report)*

Approved for public release; distribution unlimited.

17. DISTRIBUTION STATEMENT *(of the abstract entered in Block 20, if different from Report)*

18. SUPPLEMENTARY NOTES

This work sponsored by the Defense Nuclear Agency under RDT&E RMSS Code B344077464 Y99QAXSB14414 H2590D.

19. KEY WORDS *(Continue on reverse side if necessary and identify by block number)*

Constitutive Relations
Compression and Shear Wave Propagation
Impact
High Strain Rate Properties

20. ABSTRACT *(Continue on reverse side if necessary and identify by block number)*

Compression and shear wave propagation was studied in pressed polycrystalline salt. The experimentally observed longitudinal profiles and the $\Delta\sigma$-$\Delta\varepsilon$ relation obtained from these profiles were similar to the uniaxial strain data. Shear wave profiles showed very rapid attenuation with propagation. Beyond 7-8 mm depth, negligible shear particle velocities were observed. The onset of the shear signal and the observed structure in the profiles were difficult to interpret because of the experimental artifacts related to the preceding longitudinal wave.

DD FORM 1 JAN 73 1473 EDITION OF 1 NOV 65 IS OBSOLETE

UNCLASSIFIED

SECURITY CLASSIFICATION OF THIS PAGE *(When Data Entered)*

410281

JOB

20. ABSTRACT (Continued)

A material constitutive model for salt was constructed based primarily on static data. Pressure-volume relations are described by a porous solid description. An isotropic-elastic-viscoplastic-strain hardening model describes the deviator stress-strain relations. The constitutive model gave reasonable simulation of the static and dynamic uniaxial strain data. The same model predicted a strong attenuation of the shear particle velocities with propagation distance in agreement with experimental results. However, the shear wave arrival and structure observed in the experimental profiles were not matched. The present study, though limited in scope, suggests that static data on salt provide reasonable predictions under dynamic loading.

A single experiment on westerly granite gave good results. The observed shear wave amplitude was quite large and the arrival time agreed with extrapolations from ultrasonic data. The granite results suggest that compression and shear wave studies can provide useful information on dynamic strength and frictional behavior of hard rocks.

SUMMARY

An improved understanding of the dynamic strength of geologic solids surrounding an underground explosion is needed for improving calculations of the teleseismic amplitudes from these explosions. Studies of one-dimensional compression and shear waves in impacted solids have the potential for providing information that can be used to assess and extend existing material models. Of particular interest to teleseismic calculations are: direct determination of shear strength, determination of dynamic frictional characteristics along material surfaces, and determination of whether large amplitude shear waves can propagate in the materials of interest.

We chose to study polycrystalline salt, a material of interest for teleseismic calculations. We also performed two experiments on Westerly granite to get an indication of how compression and shear waves propagate in a hard rock.

Compression and shear wave experiments were conducted on pressed polycrystalline salt obtained from the Lawrence Livermore Laboratory (LLL). The uniaxial strain experiments provided results (Figure 3) similar to previous LLL work. Combined compression and shear wave experiments were then conducted to obtain longitudinal and shear particle velocity profiles. The longitudinal profiles, under combined compression and shear loading, gave profiles (Figure 5) similar to uniaxial strain profiles, indicating negligible effect of shear loading on the longitudinal stress-volume (σ_x-V) relation. Despite the small porosity (1% to 1.5%), pore-collapse was evident in the σ_x-V relations (Figure 16).

The observed shear wave profiles (Figure 6) are of low amplitude and show strong attenuation with propagation distance. Beyond about 7 mm, the shear wave amplitude is comparable to experimental uncertainities. The start of the shear wave signal and some of the structure in the profiles have not been completely explained and are most likely an experimental artifact related to the preceding longitudinal wave. When these experiments were repeated, similar results were obtained. The main conclusion from these experiments is that significant shear amplitudes cannot be propagated into salt.

A constitutive model was constructed for salt using a porous solid description for the pressure-volume relation and an isotropic strain-hardening, viscoplastic description for deviator stresses. The static model parameters are completely determined from the static data (Figures 12 and 13). The strength model parameters, determined from uniaxial stress data, give good predictions for uniaxial strain loading (Figure 14). Dynamic calculations were made using a single relaxation time in the viscoplastic model. The relaxation time was determined by matching wave profiles from one uniaxial strain experiment. Subsequent calculations with the same set of parameters gave good agreement with longitudinal profiles (Figure 17 and 18) at other stress and under combined compression and shear loading. The calculated shear wave profiles showed rapid attenuation of shear wave amplitude and strong localization of shear strain (Figure 18). These results are similar to the experimental observations. However, the structure and the arrival time do not match the experimentally observed profiles. The reasons for this mismatch are probably experimental uncertainties as indicated earlier.

A simple analysis, using the governing equations, reveals that the observed localization is a consequence of the kinematic conditions and material behavior. The localization of shear strain does not permit large shear wave amplitudes to be coupled into the specimen interior.

The main conclusions from the salt work are: the static measurements of strength are adequate for use in dynamic calculations; the small amplitude and the rapid attenuation of the shear wave, though interesting, limit the practical usefulness of combined compression and shear wave studies.

Of the two experiments on Westerly granite, one gave good results. The shear wave profiles indicate a large shear stress amplitude and an arrival time that agrees with extrapolation of ultrasonic data. The granite results suggest that compression and shear waves can be used for studying hard rocks to determine dynamic strength and friction behavior.

Based on the work done to date, it is recommended that future shear wave studies be performed on hard rocks. These studies can address the following objectives: determination of the dynamic mean stress-volume relation and determination of dynamic friction properties across interfaces. Measurements of shear particle velocity amplitudes across interfaces, at different stress levels, should be helpful in determining the role of friction under inelastic deformation.

PREFACE

This report describes the work done on a research project sponsored by the Defense Advanced Research Projects Agency under contract DNA001-76-C-0384. The project was monitored by Lt. Col. G. V. Bulin (Nuclear Monitoring Research Office).

The following persons are sincerely thanked for their contributions to this work. Discussions with D. D. Keough were very helpful throughout this work. Impact experiments were expertly constructed by D. Henley and performed by D. F. Walter. Technical assistance was provided by A. Urweider, A. Bartlett, and J. Busma. Discussions with L. Seaman were helpful in the computational work. B. Y. Lew helped with data analysis and computations.

D. B. Larson of the Lawrenece Livermore Laboratory is thanked for providing the salt core and reports on the LLL work. He is also thanked for several technical discussions.

Conversion factors for U.S. customary to metric (SI) units of measurement

To Convert From	To	Multiply By
angstrom	meters (m)	1.000 000 X E -10
atmosphere (normal)	kilo pascal (kPa)	1.013 25 X E +2
bar	kilo pascal (kPa)	1.000 000 X E +2
barn	meter^2 (m^2)	1.000 000 X E -28
British thermal unit (thermochemical)	joule (J)	1.054 350 X E +3
calorie (thermochemical)	joule (J)	4.184 000
cal (thermochemical)/cm^2	mega joule/m^2 (MJ/m^2)	4.184 000 X E -2
curie	*giga becquerel (GBq)	3.700 000 X E +1
degree (angle)	radian (rad)	1.745 329 X E -2
degree Fahrenheit	degree kelvin (K)	$t_K = (t°f + 459.67)/1.8$
electron volt	joule (J)	1.602 19 X E -19
erg	joule (J)	1.000 000 X E -7
erg/second	watt (W)	1.000 000 X E -7
foot	meter (m)	3.048 000 X E -1
foot-pound-force	joule (J)	1.355 818
gallon (U.S. liquid)	meter^3 (m^3)	3.785 412 X E -3
inch	meter (m)	2.540 000 X E -2
jerk	joule (J)	1.000 000 X E +9
joule/kilogram (J/kg) (radiation dose absorbed)	Gray (Gy)	1.000 000
kilotons	terajoules	4.183
kip (1000 ibf)	newton (N)	4.448 222 X E +3
kip/inch^2 (ksi)	kilo pascal (kPa)	6.894 757 X E +3
ktap	newton-second/m^2 (N-s/m^2)	1.000 000 X E +2
micron	meter (m)	1.000 000 X E -6
mil	meter (m)	2.540 000 X E -5
mile (international)	meter (m)	1.609 344 X E +3
ounce	kilogram (kg)	2.834 952 X E -2
pound-force (lbs avoirdupois)	newton (N)	4.448 222
pound-force inch	newton-meter (N-m)	1.129 848 X E -1
pound-force/inch	newton/meter (N/m)	1.751 268 X E +2
pound-force/foot^2	kilo pascal (kPa)	4.788 026 X E -2
pound-force/inch^2 (psi)	kilo pascal (kPa)	6.894 757
pound-mass (lbm avoirdupois)	kilogram (kg)	4.535 924 X E -1
pound-mass-foot^2 (moment of inertia)	kilogram-meter^2 (kg-m^2)	4.214 011 X E -2
pound-mass/foot^3	kilogram/meter^3 (kg/m^3)	2.601 846 X E +1
rad (radiation dose absorbed)	**Gray (Gy)	1.000 000 X E -2
roentgen	coulomb/kilogram (C/kg)	2.579 760 X E -4
shake	second (s)	1.000 000 X E -8
slug	kilogram (kg)	1.459 390 X E +1
torr (mm Hg, 0° C)	kilo pascal (kPa)	1.333 22 X E -1

*The becquerel (Bq) is the SI unit of radioactivity; 1 Bq = 1 event/s.
**The Gray (Gy) is the SI unit of absorbed radiation.

TABLE OF CONTENTS

LIST OF ILLUSTRATIONS

LIST OF ILLUSTRATIONS (Continued)

LIST OF TABLES

1. INTRODUCTION

BACKGROUND

The teleseismic amplitudes from a given underground explosion depend on the near source material properties.[1,2] Thus, numerical calculations of the teleseismic radiation field require an accurate description of the material behavior at high stresses and strain rates. In particular, the dynamic strength of the material is important in defining the extent of the inelastic region and the attenuation through this region. An improved understanding of the dynamic strength of geologic solids is the objective of the present work.

Constitutive models used to describe the behavior of near source material are based largely on laboratory data from ultrasonic, quasi-static, and shock wave experiments. Ultrasonic data provide characterization in the elastic range. Quasi-static tests (generally triaxial compression) characterize the material in the inelastic range. These tests, conducted for varying loading conditions, serve as the main input to the strength models. Shock wave data are used to assess the importance of high loading rates and provide data at stresses inaccessible by quasi-static tests. Shock data have two main restrictions:[3] the stress tensor is incompletely determined, and the loading is restricted to a particular path in strain space. Because of these restrictions, shock wave data are used indirectly; that is, material models are iteratively fitted to the wave profiles.

The loading path followed by material near an underground explosion is not the same as the loading path followed in the laboratory tests. Hence data obtained under more general loading paths, particularly under dynamic loading conditions, are desirable for assessing and extending existing material models. One method for obtaining material response under more general loading conditions is the study of one-dimensional compression and shear waves in impacted solids.[4] These studies have the

potential for providing several new pieces of information that are important to calculations of underground explosions: direct determination of shear strength to improve descriptions of dynamic strength and inelastic deformation in current material models, determination of dynamic frictional characteristics along material surfaces, and determination of whether large amplitude shear waves can propagate in the materials of interest. The last two measurements are particularly relevant to ascertaining the effects of faults and joints on wave propagation.

SCOPE OF THE WORK

Propagation of large amplitude compression and shear waves in solids is a new subject with no existing data on materials of interest. Hence the present work is of an exploratory nature. The emphasis is on data acquisition and interpreting the data in terms of a constitutive model. We chose to study polycrystalline salt, a material of interest to the teleseismic work. The specific objectives of the work were to

- Determine how compression and shear waves propagate in impact-loaded salt.
- Develop a constitutive model for salt based on existing data and check the model calculations against the experimentally observed compression and shear wave profiles.

Another material of interest to the teleseismic work is granite. To get an indication of how compression and shear waves propagated in a hard rock, we attempted two preliminary experiments on Westerly granite.

2. EXPERIMENTS

Six plate impact experiments were performed on pressed polycrystalline salt (NaCl) and two experiments on Westerly granite. The experimental method and results of these experiments are described here. All the experiments were performed using the IMPS method, described in a previous report[4] and summarized in Appendix A.

SALT EXPERIMENTS

We chose to work on the finely grained polycrystalline pressed salt used in previous static[5] and shock studies[6] performed at Lawrence Livermore Laboratory (LLL) because the study of compression and shear waves, reported here, is a new area of study. By studying a material that had been studied in the past by more conventional methods, we could draw on the past work to determine the implications of the new data. From the data acquired, we could then define future experiments on the natural salt of interest to the teleseismic work.

The salt used in our work was taken from a pressed cylinder of 12-inch diameter by 12 inches high (30.5 by 30.5 cm) supplied to us by Dr. D. B. Larson (LLL). Density and sound speed measurements on two pieces cored from the cylinder gave the following results:

Initial density (ρ_o)	=	2.135 g/cm^3
Longitudinal velocity (C_L)	=	4.48 mm/μs
Shear velocity (C_S)	=	2.64 mm/μs

Within the experimental uncertainty (2%), these values are in good agreement with the values reported in the LLL static material property work.[5]

Experimental Method

The specimens used for the impact experiments were taken from cylindrical pieces (6.35 cm diameter by 5 cm high) that were cored from the large cylindrical block. Because of the hygroscopic nature of salt,

all pieces were stored in a desiccator (or vacuum) when not in use. The cylindrical pieces were cut into thinner discs (between 2 and 4 mm thick) and were ground and lapped to provide flat and parallel surfaces. Tolerances were typically $\pm$ 0.05 mm.

Preparation of the thin discs (less than 3.5 mm) was more difficult than anticipated because the specimens tended to develop partial cracks through the specimen thickness. Careful grinding and lapping procedures were later developed to obtain the thin crack-free specimens. Thin specimens are necessary for performing multiple gage experiments.

The specimen assembly shown in Figure 1 was used in the experiments. Several thin discs (generally, three discs) were stacked together and backed by a thicker disc (5 mm or greater). The particle velocity gages consisted of thin metallic foils (U-shaped) with an active element at each specimen interface and gage leads coming out through the back. A soft aluminum ribbon, 0.001 inch thick, was bonded into an accurately machined groove (0.040 inch wide and 0.001 inch deep) on the specimen surface and pulled through the vertical holes (0.04 inch in diameter). The holes were then filled with a mixture of salt and epoxy to minimize perturbation in the propagating waves. After the gage was emplaced, the disc surfaces were lapped to ensure that the gage surface was flush with the specimen surface. The complete specimen assembly was fabricated by sequentially bonding the specimen discs using an epoxy resin. The weak cohesive strength of the pressed salt permits the use of an epoxy bond.*

From the brief description presented above, it can be seen that specimen assembly for these experiments was difficult and time consuming. However, this procedure was necessary to ensure that the gage was surrounded by the salt and to avoid gage lead artifacts.

After bonding, the assembled discs were potted in a target ring and impacted by either a PMMA or a salt flyer plate. A schematic view of the impact experiment is shown in Figure 2. Experimental measurements consisted of monitoring particle velocity time profiles at various depths in the specimen plate. In addition, projectile velocity, impact tilt, and magnetic field strengths were monitored in each experiment. The

*To avoid slippage at the interface, the interface adhesion should be higher than material cohesion.

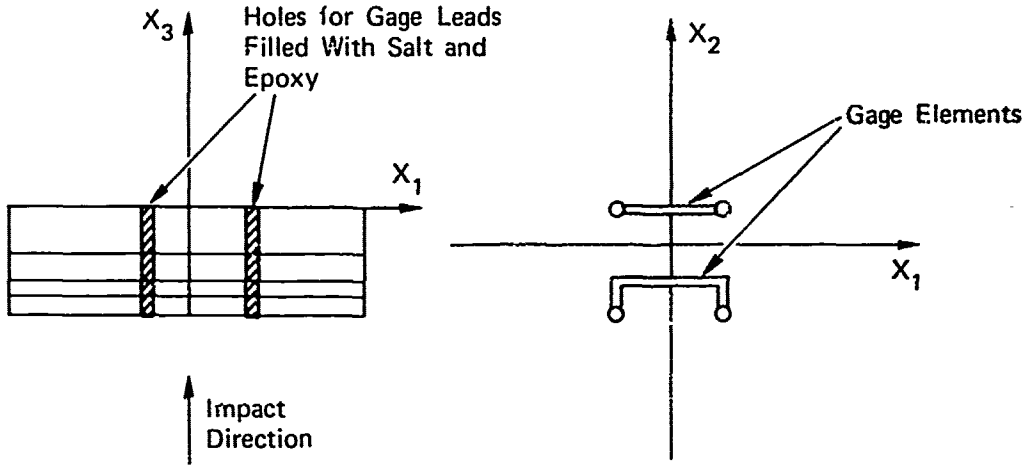

FIGURE 1 SALT SPECIMEN ASSEMBLY SHOWING THE GAGE ELEMENTS AND HOLES FOR LEADS

The three thin and thick backing plates are shown in the side view.

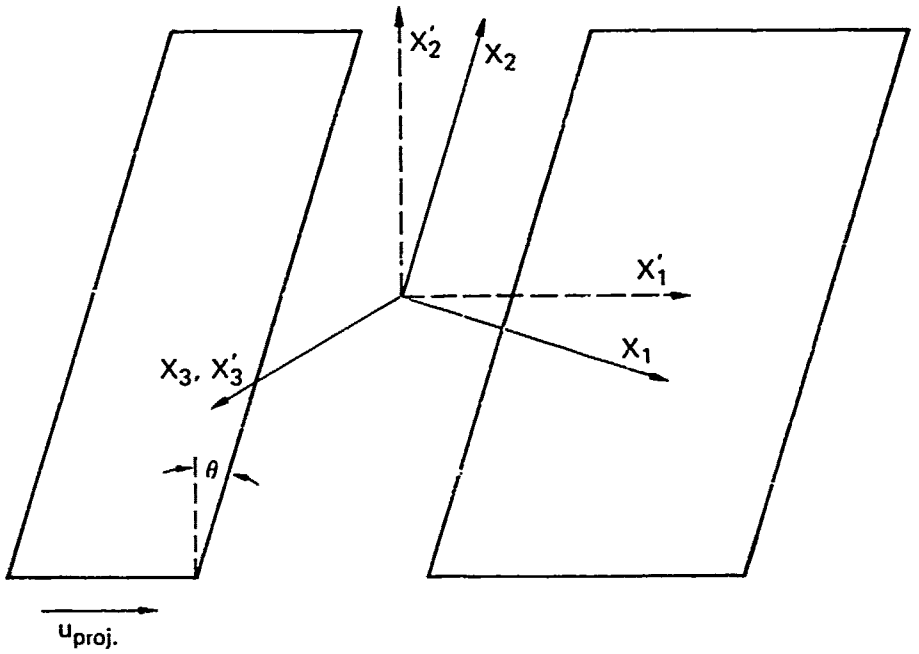

FIGURE 2 SCHEMATIC VIEW OF THE IMPACT OF TWO PARALLEL INCLINED PLATES

resul of the six impact experiments conducted on salt are discussed next These results are analyzed and compared with material model predictions in Section 4.

Table 1 lists details of the six experiments. Two types of experiments were performed: uniaxial strain (US) experiments and experiments under combined compression and shear (C + S). For the combined compression and shear experiments, the impact surfaces were inclined at 75° to the projectile axis (see Figure 2). In contrast, this angle was 90° for uniaxial strain.

Results of Uniaxial Strain Experiments

Experiment 1 (78-2-25) was a uniaxial strain experiment with a PMMA flyer plate and an impact velocity of 0.407 mm/μs. The magnetic field was aligned in the usual manner to measure the longitudinal particle velocity, $u_1(t)$. This experiment was similar to an LLL experiment. Figure 3 shows the voltage-time profiles from the five gages. Because the voltage and time scales are the same in all pictures, direct comparisons can be easily made. The gage locations were gage 1 (0 mm), gage 2 (3.79 mm), gage 3 (7.52 mm), gages 4 and 5 (11.22 mm). The leads from gages 1 through 4 came out of the side and the leads from gage 5 came out through the back. The side leads cause a small increase in signal before the arrival of the release wave, as seen in the first four records. Gages 4 and 5 show identical profiles before the small increase in gage 4.

The first gage shows a flat top signal (except for a minor perturbation at the start*) expected from the impact of PMMA on salt. The subsequent gages show a two-wave structure: a small elastic precursor followed by a large plastic wave. These profiles are in good agreement with the LLL work.[6] The following measurements were obtained from this experiment:

Peak particle velocity = 0.14 ± 0.01 mm/μs†

Elastic wave velocity = 4.33 ± 0.1 mm/μs

Release wave velocity = 4.94 ± 0.15 mm/μs

*This occurs if the gage is slightly above the surface of the specimen.

†Normally this error is 2% to 3%. The higher value quoted reflects some calibration difficulties in this particular experiment.

Table 1

DETAILS OF SALT EXPERIMENTS

Experiment No.	Experiment Type[a]	Impactor Material	Impact Velocity (mm/μ)	Particle Velocity Being Monitored[b]	Number of Gages
1. (78-2-25)	US	PMMA	0.407	u_1	5
2. (78-2-33)	US	Salt	0.409	u_2	2
3. (78-2-27)	C + S	Salt	0.412	u_1	4
4. (78-2-28)	C + S	Salt	0.409	u_2	4
5. (78-2-30)	C + S	Salt	0.412	u_1	4
6. (78-2-29)	C + S	Salt	0.412	u_2	4

[a] US denotes uniaxial strain and C + S denotes combined compression and shear.

[b] By proper alignment of the magnetic field, either $u_1(t)$ or $u_2(t)$ can be measured.

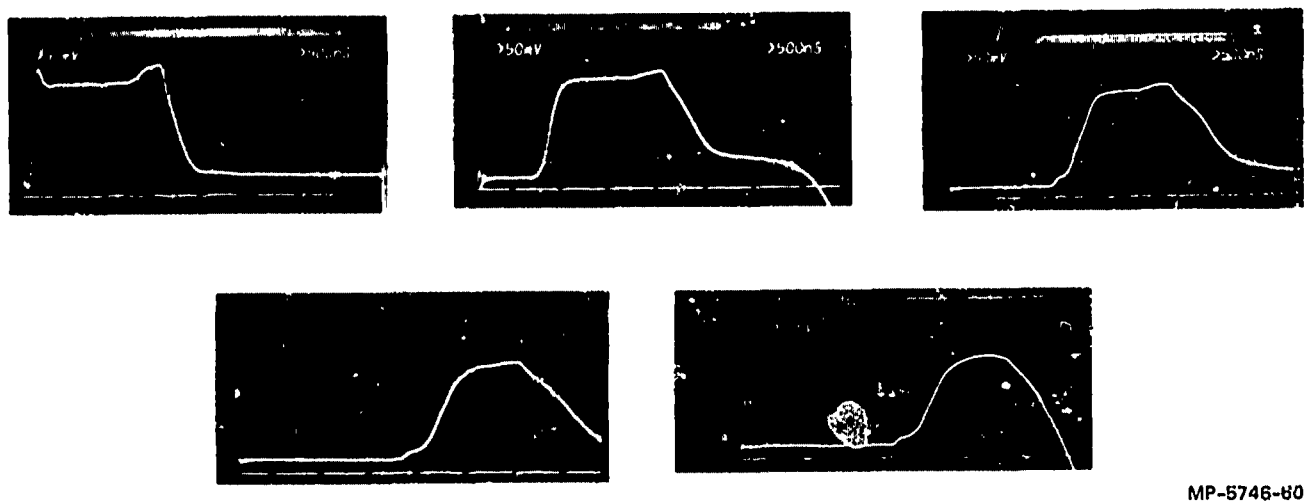

MP-5746-80

FIGURE 3 VOLTAGE-TIME PROFILES AT VARIOUS GAGE LOCATIONS (EXPERIMENT 1, 79-2-25, UNAXIAL STRAIN)

The first two values are in good agreement with the LLL work. The release wave velocity (in Lagrangian coordinates) is significantly different from the LLL value of 5.73 mm/μs.[6] Because of the procedure used in the LLL experiments, we believe that our value is more accurate.* Our value also agrees better with ultrasonic measurements in polycrystalline salt.[5] Further analysis of the profiles shown in Figure 3 are presented in Section 4.

Experiment 2 (78-2-33) was also a uniaxial strain experiment, but the magnetic field was parallel to the direction of the projectile motion. The purpose of this experiment was to determine the accuracy of our shear wave measurements described later. In a uniaxial strain experiment, only the u_1 component of particle velocity is non-zero. Hence, if the magnetic field is aligned parallel to u_1, we expect a zero signal under ideal conditions. However, because of small errors in tilt, gage emplacement, and field alignment, we can expect a small error signal. In Appendix A, we have estimated the magnitude of this signal to be 2 percent of the longitudinal signal.

To experimentally determine the magnitude of this error signal, we performed experiment 2, which was similar to our C + S shots in all respects except that it was a uniaxial strain experiment. The magnetic field strength used was the highest possible value so that it would generate as large a signal magnitude as possible. Gages were located at the impact surface and at a depth of 8.02 mm. The gage leads in this experiment, as in the C + S shots, came out through the back of the specimen. Upon exit, these leads are folded to make electrical connections. Hence the useful recording time of the gage is determined by the arrival of the wave at the rear surface. Data beyond this time are not pertinent to the results and have not been shown in any of the photographs.

---

*In the LLL work, the release wave comes from the back of the specimen and increases the particle velocity. In our work, the release wave comes from the back of the impactor and decreases the particle velocity. The decrease in particle velocity is more accurately observed than the increase because lead effects can also give rise to a small increase.

Figure 4 shows the particle velocity records from the two gages. Taking into account the baseline shifts, the impact surface gage shows a $\pm$ 13-mV signal and the interior gage shows a $\pm$ 18-mV signal. These values are comparable to the 11-mV signal estimated in Appendix A. The observed signal corresponds to a shear particle velocity magnitude that is 2% to 3% of the longitudinal particle velocity value. Hence 2% to 3% of the longitudinal particle velocity value represents the accuracy limit on the shear velocity amplitudes reported here. With additional work, the field alignment, tilt, and gage placement can be improved to reduce this error to less than a percent.

Results of Combined Compression and Shear Experiments

Experiments 3 (79-2-27) and 4 (78-2-28) were performed with the impacting surfaces inclined at an angle of 75° to the projectile axis. Both experiments had salt flyer plates and an impact velocity of 0.41 mm/μs. Each experiment had 4 gages with leads coming out of the back. For the specimen thicknesses used, a useful recording time of 3 μs after impact is obtained in these experiments. At 3 μs, the longitudinal wave reaches the back surface and the leads are perturbed.

In experiment 3 (78-2-27), the magnetic field was aligned to measure only the longitudinal component. The gage records at 0, 2.56, 5.17, and 7.62 mm are shown in Figure 5. A step input at the impact surface, resulting in a two-wave structure, can be seen in the specimen interior. The two-wave structure is less distinct than that observed in experiment 1 (Figure 3), and the plastic wave at this peak stress is much steeper than the plastic wave in experiment 1. Gage 3 in Figure 3 and gage 4 in Figure 5 are nearly at the same location, but differences in the wave profiles can be observed. The less distinct separation between the two waves and the steeper plastic wave suggest that the σ_x-V relation steepens significantly in the stress range between these shots. The trace beyond the center of the photograph is not pertinent because of lead effects discussed earlier.

In experiment 4 (78-2-28), the magnetic field was aligned to measure only the shear component. The gage records at 0, 2.12, 4.72, and 7.31 mm

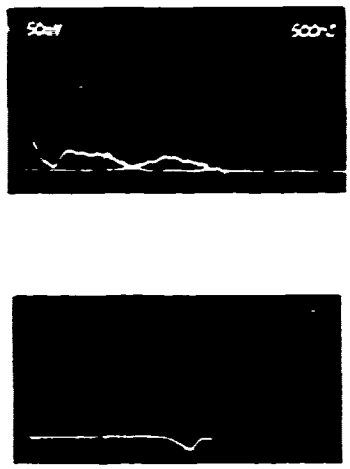

MP-5746-61

FIGURE 4 VOLTAGE-TIME PROFILES AT VARIOUS GAGE LOCATIONS (EXPERIMENT 2, 78-2-33, UNAXIAL STRAIN)

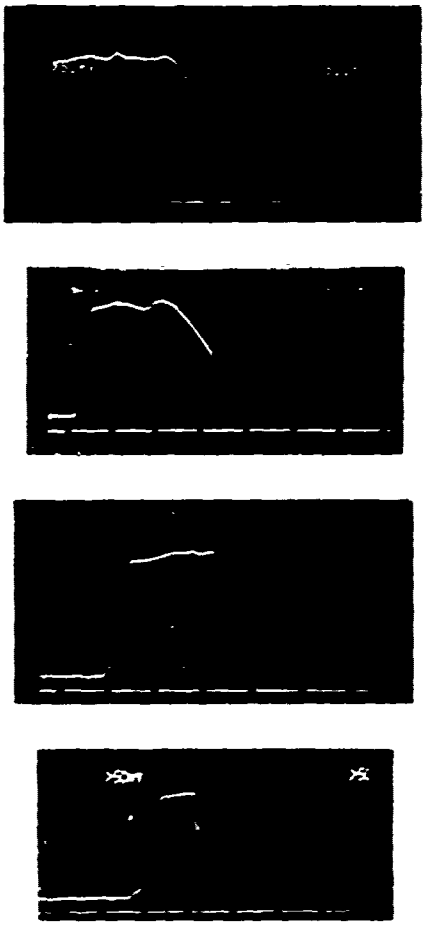

MP-5746-62

FIGURE 5 VOLTAGE-TIME PROFILES AT VARIOUS GAGE LOCATIONS (EXPERIMENT 3, 78-2-27, COMBINED COMPRESSION AND SHEAR)

are shown in Figure 6. These gage locations are similar to the gage locations in experiment 3. Data beyond the useful recording time of the gage have not been shown.

The first gage, located at the impact surface, shows the particle velocity amplitude theoretically expected from salt/salt impact and assuming no slip. The rise time is slower than in the longitudinal measurements. This result has also been observed at the impact surface in other materials and suggests that the same gage takes longer to reach peak amplitude in shear than in compression. After the peak value is reached, there is some oscillation about the peak amplitude. Although we do not have a explanation for this phenomenon, it is similar to the 'stick' and 'slip' phenomenon observed in frictional studies.[7]

The interior gages show considerably smaller amplitudes and a complex structure. Because of the small amplitude of these profiles, we first compare the amplitude of the shear signals with experimental errors determined in experiment 2 (78-2-33). To eliminate differences resulting from differences in magnetic field strengths and gage lengths, we make these comparisons by normalizing the shear wave amplitudes with respect to the longitudinal particle velocity. The first peak in particle velocities, shown in Figure 6, represent 27%, 10%, 7.5%, and 5%, respectively, of the longitudinal particle velocity imparted at the impact surface. Although the amplitude measured in gage 4 is not much larger than the 2% to 3% error observed in experiment 2 (78-2-33), the remaining amplitudes are outside the error limit.

To compare the time of arrival of the shear signal with the longitudinal wave and the ultrasonic wave velocities, we have drawn a h-t plot in Figure 7. The gage locations in the two experiments (3 and 4) were not identical, but are close enough to interpolate for accurate comparisons. In Figure 7, we show lines corresponding to the arrival of the longitudinal wave, onset of the longitudinal plastic wave, and 90% of the longitudinal peak* for experiment 3. For experiment 4, we show the onset of the shear signal and the first peak following this signal. These results give a longitudinal elastic wave velocity of

*Because of rounding, determination of the arrival time of the peak longitudinal wave is difficult and the 90% point is used.

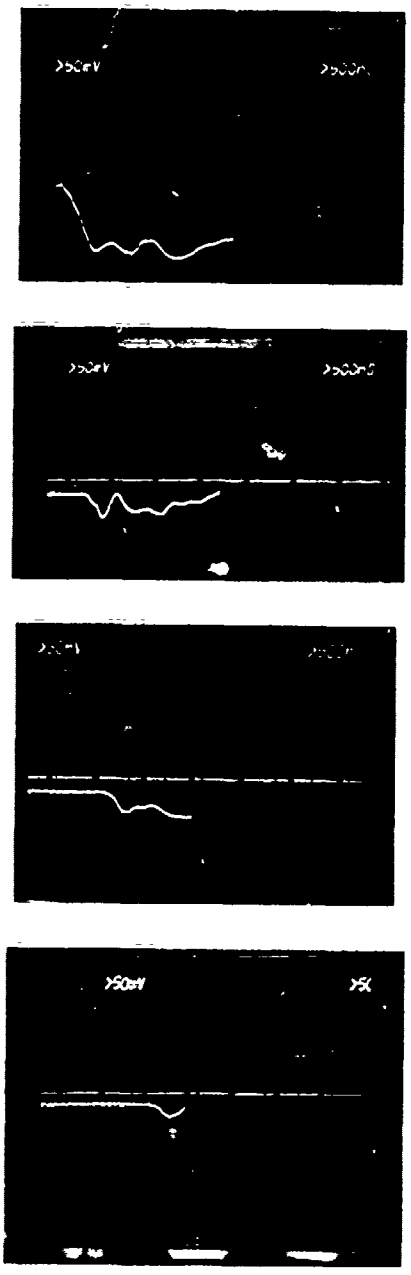

MP-5746-63

FIGURE 6 VOLTAGE-TIME PROFILES AT VARIOUS GAGE LOCATIONS (EXPERIMENT 4, 78-2-28, COMBINED COMPRESSION AND SHEAR)

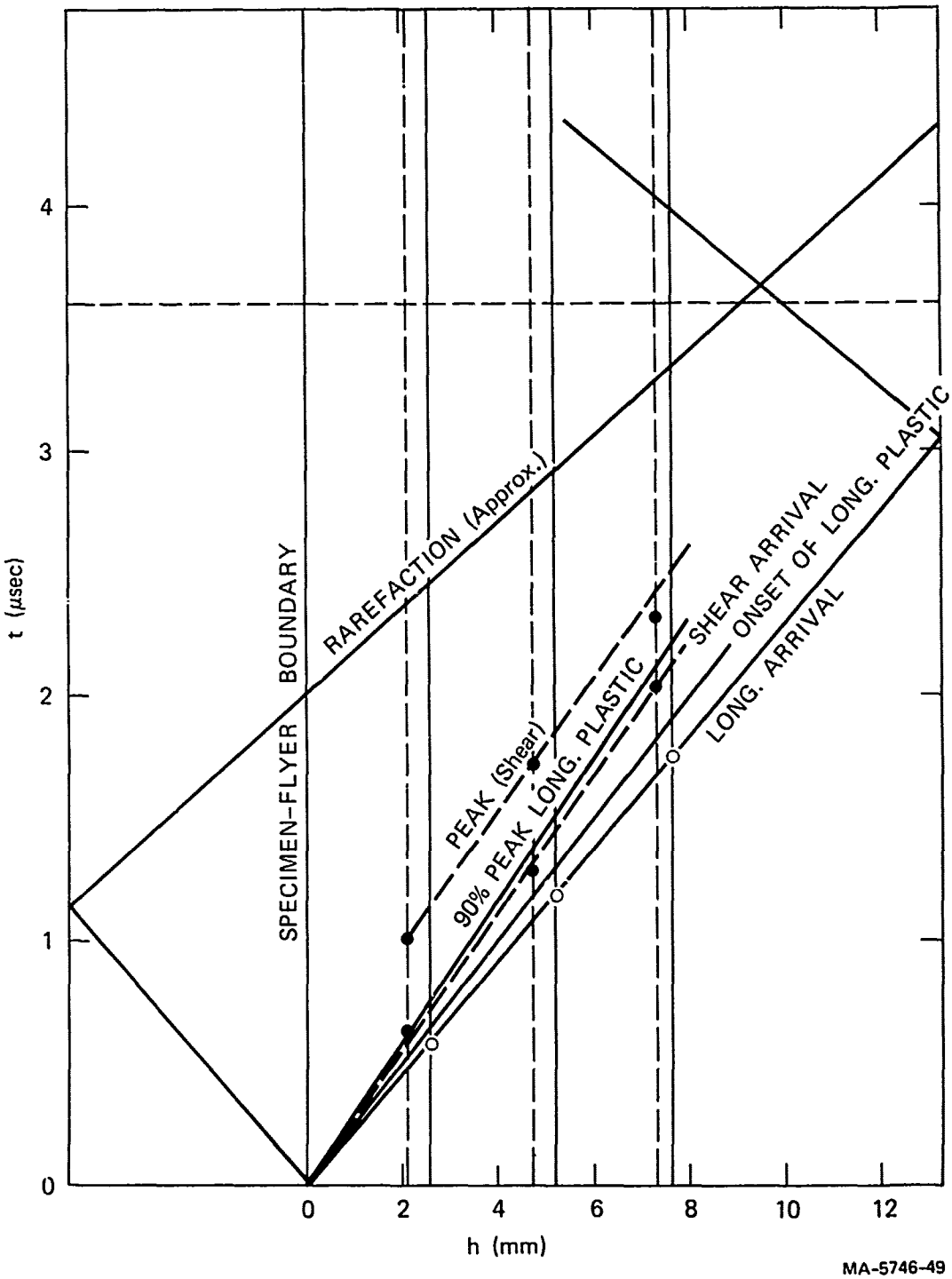

FIGURE 7 h-t PLOTS FROM EXPERIMENTS 3 AND 4.

Solid and broken lines indicate the results from the longitudinal (Experiment 3) and shear (Experiment 4) experiments respectively.

4.36 mm/μs, in good agreement with the 4.33 mm/μs measured in experiment 1. The shear wave arrival obtained from Figure 6 has a value of 3.55 ± 0.15 mm/μs and lies between the onset of the plastic wave and the 90% longitudinal peak. This value of shear wave velocity, even after correction for compression, is much higher than the ultrasonic shear wave velocities measured under static high pressure experiments.[8] It appears, therefore, that the onset of the shear signal in Figure 5 is an experimental artifact. Because of the small magnitude of the shear signal, it is not possible to get an accurate time of arrival for the shear wave. Furthermore, the structure in gage records 2 and 3 in Figure 6 makes it difficult to link a particular break in the slope with shear wave arrival. Hence the main conclusion we can draw from experiment 4 is that the shear wave amplitude attenuates very rapidly within 1-2 mm of the impact surface, and by about 7 mm, the signal amplitude is negligible.

Experiments 3 and 4 were repeated to confirm the experimental results. The results from these experiments (5 and 6) were generally similar except for the shear wave profile seen at the impact surface. Figure 8 shows the shear wave records from experiment 6. The impact surface gage shows an initial jump to the expected value and subsequently decay to a much lower value. Two possible causes for this difference are: (1) the slip conditions at the impact surface are different or (2) the gage in experiment 6 was slightly below the surface and the amplitude decays because of the rapid shear attenuation near the impact surface. At present, we cannot distinguish between these two possibilities. The interior gages show records generally similar to those shown in Figure 6. Again, no clear arrival can be noted for the shear wave.

The results from these experiments can be summarized as follows: the longitudinal wave profiles under combined compression and shear are similar to the uniaxial strain profiles; the shear wave profiles show very large attenuation in amplitude near the impact surface, and very little shear motion is coupled into the specimen interior. The accurate determination of shear wave arrival is not possible from the present data. The rapid shear wave attenuation is discussed further in Section 4 and compared with the material model predictions.

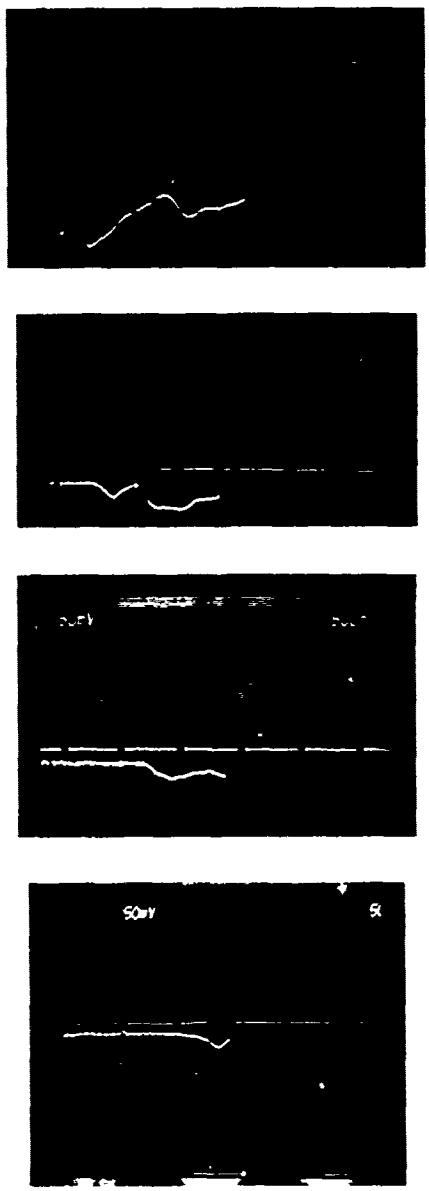

MP-5746-64

FIGURE 8 VOLTAGE-TIME PROFILES AT VARIOUS GAGE LOCATIONS (EXPERIMENT 6, 78-2-29, COMBINED COMPRESSION AND SHEAR)

GRANITE EXPERIMENTS

The purpose of the granite experiments was to determine the feasibility of propagating and measuring large amplitude compression and shear waves in a hard rock. Two experiments, with different gage emplacement techniques, were performed. Only one of these was successful and is described below (Proj. Vel. = 0.41 mm/μsec, Angle θ = 12°).

Experimental Method

The experimental assembly for the granite shot was similar to that for the salt shots. Particle velocity gages were inlaid in the material with gage leads coming out of the back as shown in Figure 1. Copper wires (0.002 inch in diameter) instead of aluminum foils were used as gage elements. These small wires were connected to 0.03-inch-diameter copper wires, which served as gage leads. The space around the gage element and gage leads was filled with aluminum Devcon* to minimize perturbation in the wave front. The granite discs were not bonded together with epoxy like the salt discs, but were mechanically pressed together and potted in the aluminum ring. It was felt that the adhesion strength caused by friction between the granite pieces would be stronger than the cohesive and/or adhesive strength of the epoxy.

Because we were able to perform only one experiment, we wanted to observe signals from both the longitudinal and shear wave. This was accomplished by using a magnetic field configuration that gives rise to a signal from each wave. The longitudinal and shear signals are distinguished by the arrival time of the two waves. This approach to distinguishing the two waves is applicable only when distinct and large signals are expected from each wave, unlike the salt results. As discussed next, the signals from the granite experiment were indeed large enough to permit this distinction.

Experimental Results

The particle velocity profiles from the three gages are shown in Figure 9. As expected, these records display substantial piezoelectric noise. The first gage shows a square wave input, the second gage starts to show a wave separation, and the third gage clearly shows the two-wave structure: compression and shear wave.

*A commercially available mixture of aluminum and epoxy.

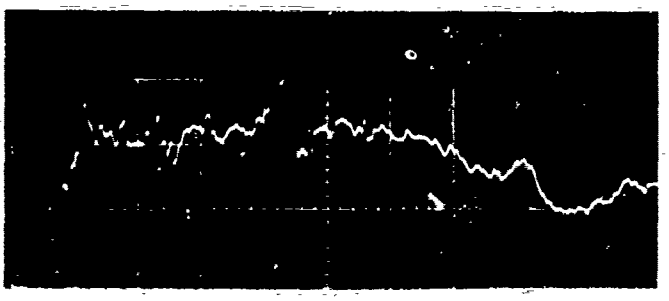

(a) 0 mm

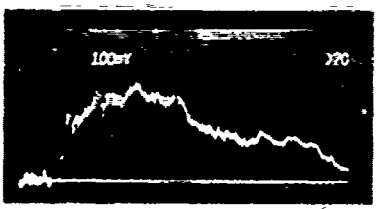

(b) 2.54 mm

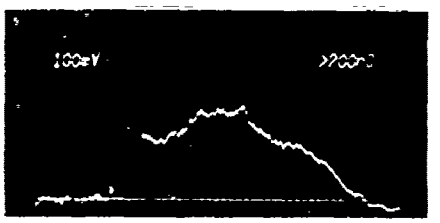

(c) 5.08 mm

MP-5746-65

FIGURE 9 VOLTAGE-TIME PROFILES AT VARIOUS GAGE LOCATIONS IN THE GRANITE (COMBINED COMPRESSION AND SHEAR)

Figure 10 shows the voltage-time signal from gages 1 and 3 along with the signal expected from the granite for a no-slip, elastic response. The plots in Figure 10(a) show that the measured signal is in good agreement with the expected signal for a symmetric no-slip impact; that is, the shear velocity transmitted to the specimen is one-half the projectile velocity along the shear direction. The plots in Figure 10(b) show that the first wave amplitude agrees with the expected longitudinal signal. However, the second wave amplitude is slightly smaller and considerably more dispersive than that expected from an elastic response. The amplitude of the shear wave is a measure of the dynamic strength, and the wave profile shape indicates a convex shear stress-strain relation.

The wave velocities used in generating the elastic profiles in Figure 10 are: a longitudinal wave velocity of 5.35 ± 0.25 mm/μs measured in these experiments and a shear wave velocity of 3.67 mm/μs obtained from extrapolation of ultrasonic data.[4]

Because of the quality the records, further analyses were not attempted. The main conclusions from the granite shot are that compression and shear waves can be propagated and measured in hard rocks. By extending the stress range to higher values, we can determine the shear stresses that cause shear failure and find out about the post-failure behavior of the solid. In addition, the measurement of shear wave velocity in the shocked state can allow direct determination of the mean stress-volume relation in the shocked state, as discussed in Section 4. These measurements in hard rocks may also allow us to obtain new information regarding dynamic inelastic deformation (see Section 4). Future effort, however, should focus on a hard rock without the piezoelectric noise to allow more accurate investigation of material effects.

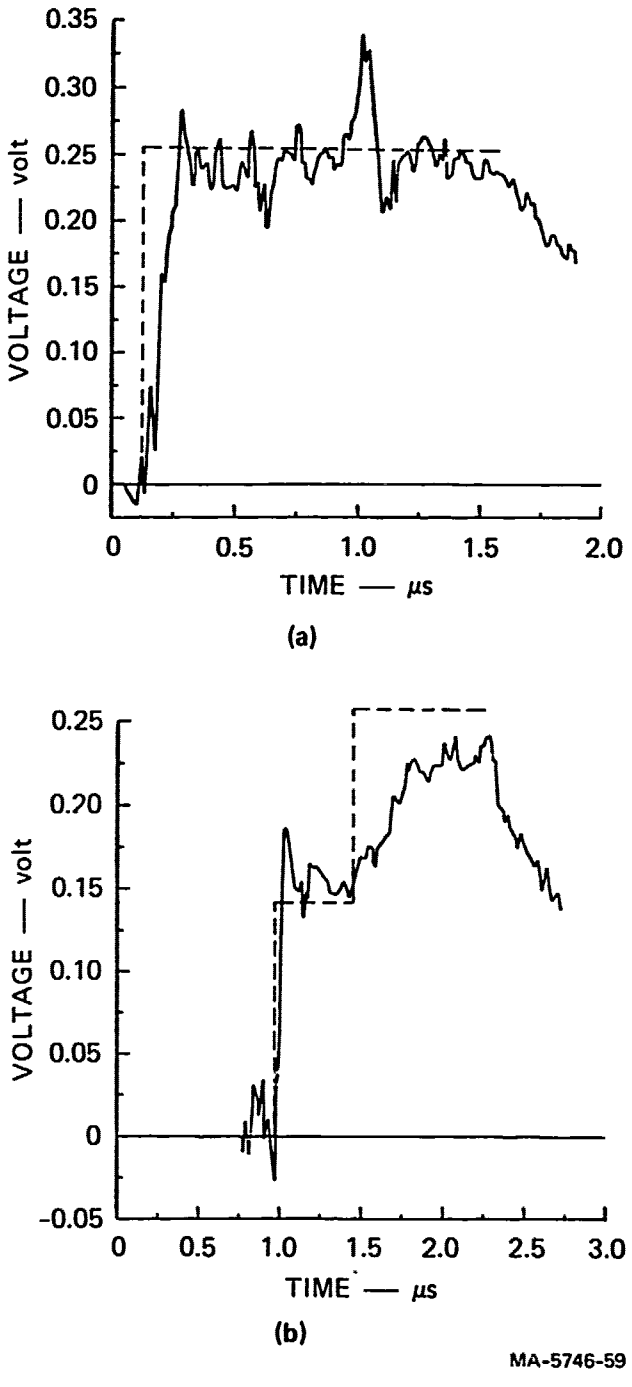

FIGURE 10 COMPARISON OF SIGNAL DETERMINED FROM LINEAR ELASTIC CONSIDERATIONS AND MEASURED SIGNAL

3. CONSTITUTIVE MODEL FOR SALT

An important objective of the present work was to develop a mechanical constitutive model for salt. Static, ultrasonic, and plate impact uniaxial strain data obtained at LLL[5,6] provided the basis for the form of the constitutive relations and the specific material parameters. These constitutive relations were used to calculate wave profiles under combined compression and shear loading for comparison with experimental data obtained in the present work. These comparisons are presented in Section 4.

This section presents the main features of the constitutive relations and the determination of the material parameters. Detailed derivation of the equations and incorporation into the wave propagation code are given in Appendices B and C.

FORMULATION OF THE MODEL

In choosing the constitutive description, we concentrated on using the simplest continuum model that would incorporate the experimentally observed features. The main elements of the model were determined from the static data with later modifications for incorporating plate impact data. This approach was used because the static data are more complete than the dynamic data.

During deformation, salt displays many features typical of metal plasticity: elastic-ductile plastic deformation, strain-hardening, and lack of dilatant behavior.[5] While porosity effects* need to be included in the constitutive relations, the small amount of porosity permits considerable simplification. The effect of shear on the pressure-†

*The salt specimens obtained from LLL have 1% to 1.5% porosity.

†We use 'pressure' to denote the negative of mean stress. For purely hydrostatic loading, 'pressure' will be replaced by 'hydrostatic-pressure.'

volume relation is small and can be approximated by using the pressure-volume relation obtained from static uniaxial strain data. Shear-enhanced compaction need not be explicity incorporated in the pressure-volume relation and in the subsequent calculations. The thermal effects of pore-collapse and yielding are also ignored in the present work.

Because of the above considerations, the pressure and deviator parts of the constitutive relation can be uncoupled and determined separately,

$$\sigma_{ij} \equiv \frac{\sigma_{mm}}{3} \delta_{ij} + \sigma'_{ij} \qquad (1)$$

where $\sigma_{mm}/3$ is the mean stress or pressure and σ'_{ij} are the stress deviators. Forms of the equations describing the stress-strain relations for each of these two parts are presented in the next two subsections.

Of the various materials of interest to the DARPA teleseismic program, salt comes closest to a metal in terms of its deformation behavior. This similarity simplifies the constitutive description.

PRESSURE-VOLUME RELATION

Although the porosity of the salt being studied is small (1% to 1.5%), both static and dynamic data show pore-compaction effects.[5,6] Hence the pressure-volume relation should incorporate pore-collapse and consolidation to the solid material. Of the various models used to describe porous solids, we chose the empirical relation presented in Seaman's work on radiation deposition in porous metals.[9] By neglecting thermal effects, we have further simplified this model for our purposes. A brief description of Seaman's model is presented below. A listing of the porous P-V model, subroutine POROUS1, and a flow chart demonstrating how the equations (which are presented later) are used in the numerical calculations are given in Appendix B along with the procedure for inserting POROUS1 into the COPS code.

Figure 11 shows the pressure-volume relationship typically observed for a porous solid. As will be shown later, a similar form is observed for salt. To describe the pressure-volume relation shown in Figure 11, we consider initial loading in the porous state (path ABC), unloading and reloading in the porous state (BD), and unloading and loading in the solid state (CF).

Loading in the porous state (curve ABC) is characterized by an initial elastic response,* pore-compaction, and consolidation to the solid material. In our model, we assume that the mean stress-volume relation of the porous solid after consolidation is identical to that of the nonporous material. This assumption is only an approximation but is reasonable within our use of the model.† In the model, curve ABC in Figure 11 is defined as a series of parabolic segments. A three-segment approximation to curve ABC is shown in Figure 11. Each segment is defined by an equation of the form

$$P = P_i + \frac{P_{i+1} - P_i}{V_{i+1} - V_i}(V - V_i) - \frac{4DP}{(V_{i+1} - V_i)^2}(V - V_i)(V - V_{i+1}) \quad (2)$$

where, V is the specific volume and the subscripts i and i+1 denote quantities at the beginning and end of a segment, respectively. The second term on the right hand side of Equation (2) represents a linear P(V) variation between V_i and V_{i+1}, and the quantity DP is the maximum deviation from this linear curve. In segments 1, 2, and 3 of Figure 11, DP is positive, zero, and negative, respectively.

Equation (2) was derived by assuming a P(V) variation of the form

$$P = a + b(V - V_i) + c(V - V_i)(V - V_{i+1}) \quad (3)$$

---

*Elastic implies no pore-compaction.

†If thermomechanical effects are included, the P-V-E surface of the porous and solid material will not be coincident in the P-V plane.

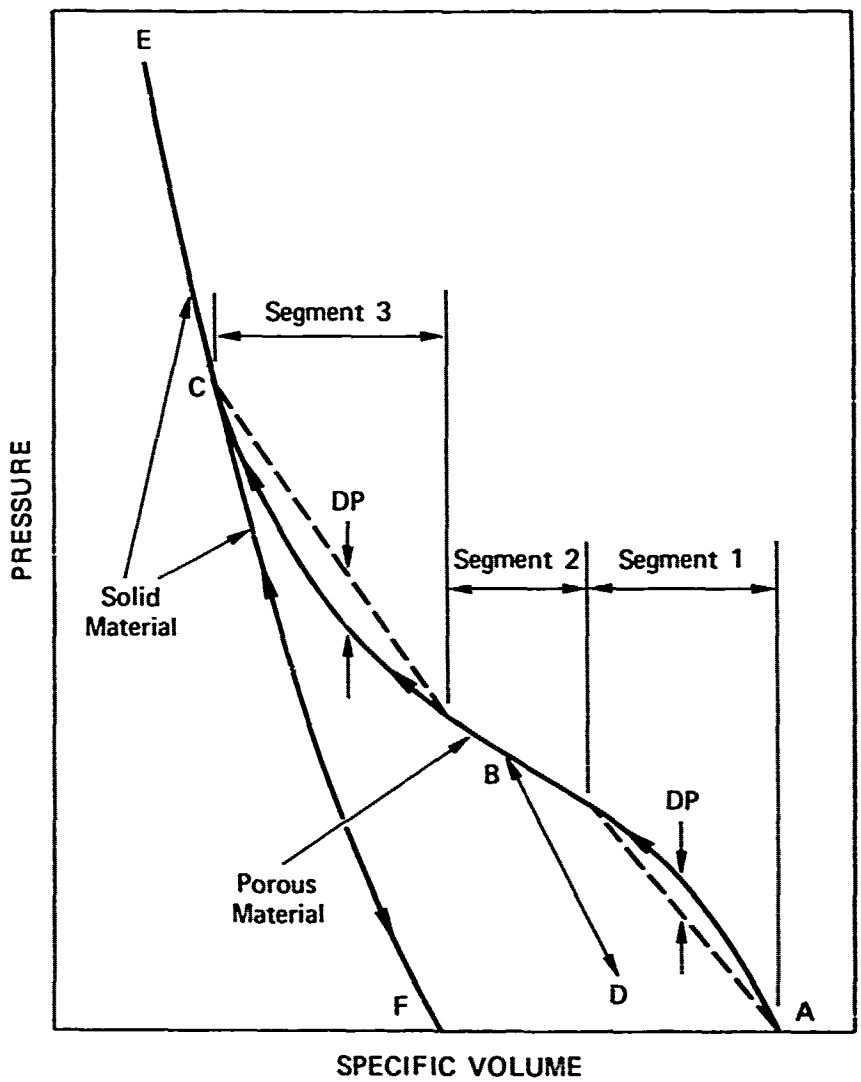

FIGURE 11 PRESSURE-VOLUME RELATION FOR A POROUS MATERIAL

ABC describes the porous loading curve and FCE describes the solid curve.

for a segment. The constants a and b were determined by requiring that $P(V_i) = P_i$ and $P(V_{i+1}) = P_{i+1}$; the constant c was obtained by solving for the location of the extremum of the quadratic term of Equation (3). This is the procedure used by Seaman to model the initial loading portion of a porous material P-V relationship and is described in detail in reference 9. By proper choice of segments, the changes in slope at segment joints are minimized.

Unloading from a partially consolidated state (path BD) is assumed to be elastic, that is, no change of porosity. The unloading path is given by

$$\Delta P = K \frac{-\Delta V}{V_{avg}} \tag{4}$$

where

ΔP and ΔV = pressure and specific volume increments

V_{avg} = average of the specific volumes at the beginning and end of a cycle

K = bulk modulus between the initial and consolidated states defined as

$$K = K_I + \frac{K_c - K_I}{\rho_c - \rho_I} (\rho_{avg} - \rho_I) \tag{5}$$

where

K_I and K_c = bulk moduli in the initial and consolidated states

ρ_I and ρ_c = initial and consolidated densities

ρ_{avg} = average of the densities at the beginning and end of a cycle.

Reloading occurs elastically along the same path until the original loading curve is reached. Curve BD in Figure 11 represents a typical unloading/reloading path in a partially consolidated state.

If the pressure is high enough, all the porosity is expected to be eliminated. This consolidation is described in the model by prescribing a consolidation density ρ_c (Point C in Figure 11). Once this

density is exceeded, loading and unloading occur along the solid P-V relation, curve ECF in Figure 11. The solid curve in our model is described by the relationship

$$P = A\mu + B\mu^2 \tag{6}$$

where

A = bulk modulus of solid material at ambient pressure

$\mu = \rho/\rho_{so} - 1$; ρ_{so} = density of solid material at ambient pressure

B = coefficient of term describing monlinear behavior.

The above pressure-volume relation is consistent with a linear relationship for bulk modulus

$$K = K_o + \alpha P \qquad \text{if} \quad \alpha = 1 + \frac{2B}{A} \tag{7}$$

The form of Equation (6) is consistent with hydrostatic pressure-volume measurements made in polycrystalline salt.[10]

The material parameters required for specifying the pressure-volume relation are:

- Bulk modulus and density of the porous material at ambient pressure (K_I and ρ_I).
- Bulk modulus and density of the porous material at the consolidation point (K_c and ρ_c).
- Bulk modulus and density of the solid material at ambient pressure (K_{so}, ρ_{so}) and P-V relation for the solid material.
- Parameters for the parabolic segments describing the porous loading curve ABC in Figure 11.

The determination of these parameters from the experimental data of Heard et al.[5] is described next* and summarized in Table 2.

Table 2

PARAMETERS FOR POROUS MATERIAL MODEL

Material parameters	
Bulk modulus of porous material at ambient pressure	K_I = 225 kbar (22.5 GPa)
Bulk modulus at consolidated density	K_c = 274 kbar (27.4 GPa)
Coefficient of linear term in the P-μ relation for solid material	A = 245 kbar (24.5 GPa)
Parameters defining porous material mean stress-volume path	
P_1 = 0 or ambient	V_1 = 0.4675 cm^3/g
P_2 = 0.802 kbar	V_2 = 0.4652 cm^3/g
P_3 = 2.31 kbar	V_3 = 0.4605 cm^3/g
P_4 = 5.70 kbar*	V_4 = 0.4535 cm^3/g*
DP_1 = -0.1 kbar	
DP_2 = 0.12 kbar	
DP_3 = -0.3 kbar	

*Consolidation values.

A ρ_I value of 2.139 g/cm^3 was used in our calculations. The K_I value was obtained from the ultrasonic data of Heard et al. (Figure 9 in Reference 5). Beyond a confining pressure of 25 MPa, a straight line can be drawn through the K-P results obtained from their ultrasonic

*Our density and sound velocity measurements (Section 2) on the salt cores are similar to those of Heard et al.[5] We will therefore assume that all of their measurements are applicable to our cores.

measurements. This straight line was extrapolated to P = 0 and provided a value of K_I = 225 kbar (22.5 GPa). At the consolidation point, the bulk modulus and density of the porous material are the same as for the solid material and are described below.

The initial bulk modulus and density of the solid material are the values cited by Simmons and Wang.[11] These are K_{so} = 245 kbar and ρ_{so} = 2.16 g/cm^3.* Using these values, we fitted a quadratic relation, as given in Equation (6), to Decker's data on polycrystalline salt.[10]

$$P = 245\mu + 505.3\mu^2 \text{ kbar} \qquad (8)$$

The pressure-volume curve for the porous solid is obtained by fitting parabolic segments to the mean stress-volume curve obtained under static uniaxial strain loading. As explained earlier, this procedure approximates the effect of shear deformation on compaction. Three parabolic segments were used to fit the loading curve; the material parameters describing these segments are presented in Table 2. The porous and solid loading curves used in our work are shown in Figure 12. The consolidation point is given by P_4 = 5.7 kbar and V_4 = 0.4535 cm^3/g. Beyond this point, the material loads and unloads along the solid curve.

For the porous material, the unloading and reloading path is specified by the bulk modulus.† This requires values for K_I and K_c (bulk modulus at consolidation). A value of K_c = 274 kbar is obtained by using Equation (7) and the P_c value cited above. The bulk modulus at an intermediate point is provided by linear interpolation.

---

*To get a good match with the porous data, we used ρ_{so} = 2.157, instead of 2.16.

†In the porous region, the bulk modulus does not define the loading modulus.

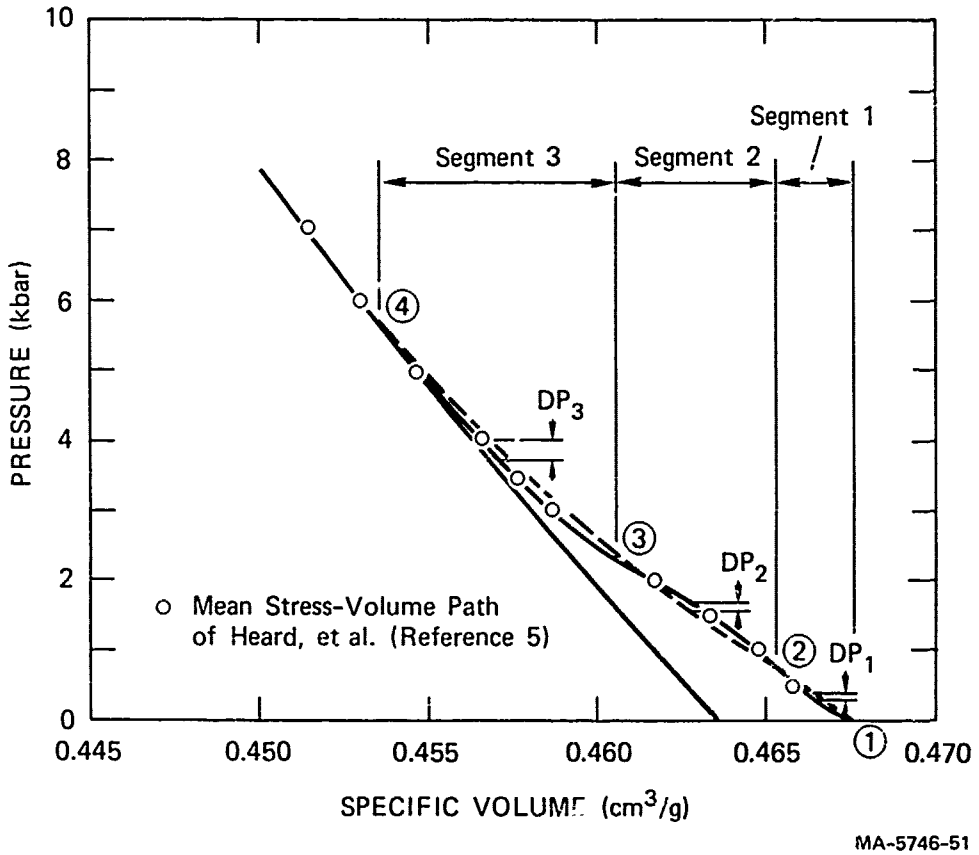

FIGURE 12 POROUS AND SOLID MATERIAL MODEL LOADING PATH

DEVIATOR STRESS DESCRIPTION

Heard et al. have performed static uniaxial stress* and uniaxial strain experiments on salt.[5] Their data provide the basis for the deviator stress (or strength) model in our work. We first discuss their results and then describe the constitutive model. A detailed derivation of the equations and the insertion of the deviator stress subroutine into the COPS code is presented in Appendix C.

Data from uniaxial stress experiments show a brittle-ductile transition at a confining pressure of 10 bars.[5] Beyond this value, the increase in strength with pressure is negligible. During loading, the material displays yield followed by strain hardening. Unloading in these experiments is elastic and results in a small amount of net compaction caused by the small porosity present in the salt. Unlike other geologic solids of interest, salt deforms like a metal with the following characteristic features: distinct yield, nonlinear strain hardening, negligible dependence of yield strength of pressure, and no dilatancy.

The uniaxial strain data plotted by Heard et al.[5] show increasing shear strength with confining pressure when plotted in stress space. This strength increase is deceptive because the deviatoric strains are also increasing with compression. When transformed to a deviator stress-strain plot, these data show strain hardening somewhat similar to that observed in the uniaxial stress experiments.

Based on these results, the following elastic-plastic model with isotropic strain hardening is used to represent the deviator stress-strain relations.

(1) Additivity of incremental elastic and plastic strains

$$d\varepsilon_{ij} = d\varepsilon_{ij}^{e} + d\varepsilon_{ij}^{p} \tag{9}$$

---

*This classification also includes tests in which the axial stress is superposed on a constant confining hydrostatic pressure.

(2) Incremental Hooke's law

$$d\sigma'_{ij} = 2Gd\varepsilon'_{ij} \tag{10}$$

where $d\varepsilon'_{ij} \equiv d\varepsilon_{ij} - \frac{d\varepsilon_{mm}}{3}\delta_{ij}$

(3) Yield surface of the von-Mises type with strain hardening

$$f = \sqrt{J'_2} - Y = 0 \tag{11}$$

where $\sqrt{J'_2} = \sqrt{\frac{1}{2}\sigma'_{ij} \cdot \sigma'_{ij}}$

and $Y = Y_o + g(\varepsilon^p_{ij})$

(4) Plastic incompressibility

$$d\varepsilon^p_{mm} = 0 \tag{12}$$

G is the shear modulus and is a function of pressure; g is a strain-hardening function to be determined from the experimental data.

The above equations are the usual relations presented in a continuum plasticity textbook.[12] Given the available experimental data on salt, these equations are quite adequate as will be seen in the next section.

The above equations represent a model that is suitable for describing static tests. For simulating impact experiments, we need to incorporate a rate dependent or viscoplastic model. The model used here is similar to the overstress model discussed by Perzyna.[13] The stresses beyond yield are given by

$$\sigma'_{ij} = (\sigma'_{ij})_I \left[1 - \left(\frac{\sqrt{J'_{2I}} - \sqrt{J'_{2E}}}{\sqrt{J'_{2I}}}\right)\frac{\Delta t}{T_r}\right] \tag{13}$$

The subscripts I and E denote the instantaneous and equilibrium values as discussed below; Δt and T_r are the time step and relaxation time, also explained in the following. In a rate-independent problem, stress states outside the yield surface, that is, $f > 0$, are not permissible. The magnitude of the plastic strain is determined by the condition that $df = 0$. For a viscoplastic model, stress states $f > 0$ are permissible and the stresses relax toward the current value of the static yield surface Y (equilibrium value) with a relaxation function proportional to the stress overshoot and a relaxation time T_r. The instantaneous stress $(\sigma'_{ij})_I$ is defined as

$$(\sigma_{ij})'_I = (\sigma_{ij})'_o + 2G\,\Delta\varepsilon'_{ij} \tag{14}$$

where $(\sigma'_{ij})_o$ is the deviator stress at the start of the increment and $\Delta\varepsilon'_{ij}$ is the deviatoric strain increment* in a time step Δt. The corrected stresses at the end of the increment are given by σ'_{ij}, and the plastic strain increments are given by

$$\Delta\varepsilon'^{p}_{ij} = \frac{(\sigma'_{ij})_I - \sigma'_{ij}}{2G} \tag{15}$$

For $\Delta t/T_r \ll 1$, Equation (13) gives $\sigma'_{ij} \simeq (\sigma'_{ij})_I$, and for $\Delta t/T_r = 1$, $\sigma'_{ij} = (\sigma'_{ij})_E$. For $\Delta t > T_r$, the stresses are set equal to $(\sigma'_{ij})_E$. Related forms for Equation (13) may be seen in studies by Seaman[14] and Johnson.[15]

For a perfectly plastic material (including pressure-dependent strength), the use of Equation (13) is quite straightforward because the yield surface is fixed in stress space. In the presence of strain hardening, the determination of σ'_{ij} and $\Delta\varepsilon'^{p}_{ij}$ is complicated because of changing Y. However, a closed form solution within an increment has been obtained. Details of this derivation are given in Appendix C; here we present the results of this derivation.

---

*Assumed elastic for computing $(\sigma'_{ij})_I$.

We have chosen a strain-hardening model given by

$$Y = Y_o + M \sqrt{\Delta I_2'^P} \tag{16}$$

where $\sqrt{\Delta I_2'^P} \equiv \sqrt{1/2 \; \overline{e_{ij}'^P \cdot \Delta\varepsilon_{ij}'^P}}$ and Y_o is the yeild stress at the start of the increment. M is a nonlinear function and depends on the current value of the accumulated plastic strain ε_{ij}^P. $\sqrt{J_{2E}'}$ in Equation (13) is the same as Y.

$$\sqrt{J_{2E}'} = {}^o\sqrt{J_{2E}'} + M\sqrt{\Delta I_2'^P} \tag{17}$$

The first term on the right side is the equilibrium stress at the start of the increment. The above equations can be combined to give

$$\sqrt{\Delta I_2'^P} = \frac{\sqrt{J_{2I}'} - {}^o\sqrt{J_{2E}'}}{M + \dfrac{2GT_r}{\Delta t}} \tag{18}$$

Because all the terms on the right side of Equation (18) are known, we can obtain $\sqrt{\Delta I_2'^P}$. Then Equations (17), (13), and (15) can be evaluated to give all the stresses and strains.

The material parameters for the deviator stress model are:

- Shear modulus G and its dependence on pressure P.
- Initial value of yield stress and the strain hardening relation.
- Relaxation time, T_r.

We consider the first two items here and postpone determination of T_r to Section 4.

The shear modulus was assumed to vary linearly with pressure,

$$G = G_o + G_1 P \tag{19}$$

For G_o, we used a value of 13.7 GPa (137 kbar) given by Heard et al. (Table 3 of Reference 5). A G_1 value of 0.22 GPa (2.2 kbar) was

determined by taking the slope of the shear modulus-pressure curve (Figure 9 in Reference 5).

An initial yield stress value, Y_o = 25.4 MPa, was obtained from the quasi-static uniaxial stress data (Figure 4 in Reference 5). Stress difference ($\sigma_1 - \sigma_3$) versus axial strain (ε_1) and radial and hoop strains ($\varepsilon_2 - \varepsilon_3$) curves obtained from these data were used to construct the strain-hardening curve ($\sqrt{J_2'} - Y_o$ versus $\sqrt{I_2'^P}$) shown in Figure 13. This curve was fitted by a series of parabolic segments in a manner similar to that used for the porous model. The parameters corresponding to the six segments are given in Table 3. Segment 6 and part of segment 5 are not shown in Figure 13 because the strain-hardening curve in this region is nearly a straight line.

Table 3

PARAMETERS DEFINING THE STRAIN-HARDENING CURVE

$\sqrt{J_{2E}'} - Y_o$ (kbar)	$\Delta[\sqrt{J_{2E}'} - Y_o]^*$ (kbar)	$\sqrt{I_2'^P}$
0.0	0.0	0.0
0.05197	0.007	0.000965
0.10393	0.01366	0.0042395
0.195	0.004	0.021223
0.218	0.0	0.037882
0.22	0.0	0.068
0.22	0.00	1.0

*$\Delta[\sqrt{J_{2E}'} - Y_o]$ is the maximum deviation from a linear $\sqrt{J_{2E}'} - Y_o$ versus $\sqrt{I_2'^P}$ variation.

SIMULATION OF STATIC DATA

The strength model parameters presented in the previous subsection were determined from the uniaxial stress data. Hence no attempt was made to simulate the uniaxial stress experiments. Instead, we simulated

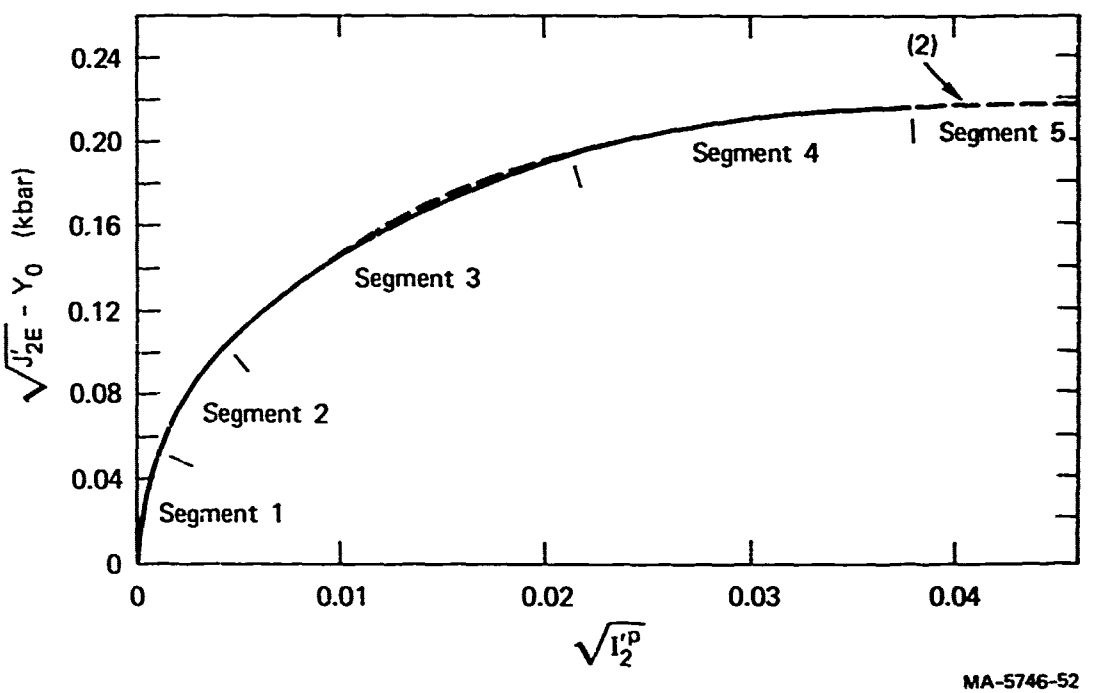

FIGURE 13 STRAIN-HARDENING CURVE (SOLID LINE) OBTAINED FROM THE DATA OF HEARD ET AL.

The dotted line shown in segments 3 and 5 is the curve actually used.

the uniaxial strain data. This simulation provides a good check of the strength model because it exercises the model for a different test condition.

The uniaxial strain experiment is simulated using a test program that imposes one-dimensional strain increments to the desired peak strain value. From a knowledge of the strains, the stresses are calculated using the material model routines POROUS1 (P-V relation) and VPSH (deviator stress-strain relation). The listings for these routines are given in Appendices B and C. This simulation is similar to the use of material property subroutines in the wave propagation code.

Figure 14 compares the calculations with the experimental measurements of Heard et al.[5] Figure 14(a) shows the plots for σ_1 versus V/V_o, and Figure 14(b) shows the plots for $\sigma_1 - \sigma_3$ versus σ_3. The agreement is generally quite good except over the stress range in which pore-collapse predominates. The experimental data show that a strength decrease accompanies pore-compaction. However, in our model no such interaction exists between pore-compaction and material strength. Because of the complexity in describing this interaction, no attempts were made to include it in the material model. As remarked earlier, the increase in $\sigma_1 - \sigma_3$ with increasing σ_3 is misleading because the real reason for this increase is strain hardening and not pressure dependence. From this simulation, we conclude that the strength model is satisfactory for calculations along other load paths.

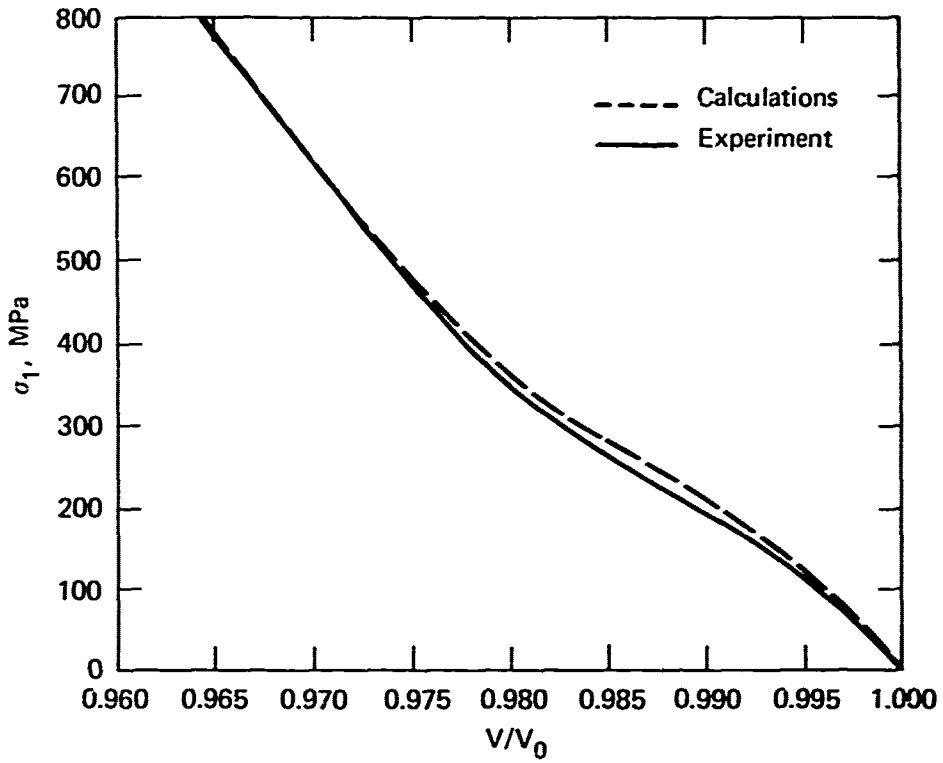

(a) σ_1 VERSUS V/V_0

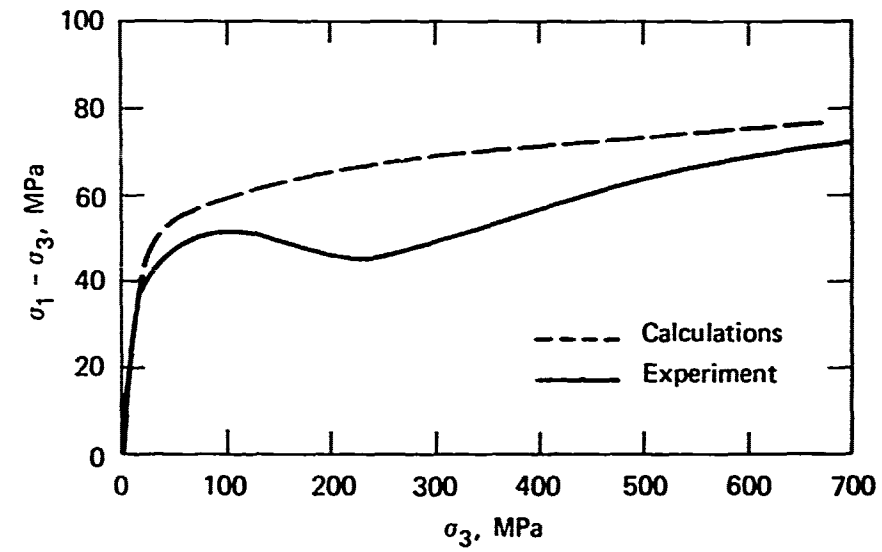

(b) $\sigma_1 - \sigma_3$ VERSUS σ_3

MA-5746-53

FIGURE 14 COMPARISON OF THE CALCULATED AND EXPERIMENTALLY MEASURED CURVES FOR STATIC UNIAXIAL STRAIN LOADING

4. ANALYSES AND CONCLUSIONS

In this section we analyze the data presented in Section 2. First the longitudinal profiles are analyzed to give the longitudinal stress-volume results. This is followed by a numerical simulation of the wave profiles and comparison with experimental data. Next, the rapid decay of shear wave amplitude is discussed by analyzing the equations governing wave propagation. Some concluding remarks, including directions for future work, are presented at the end of the section.

LONGITUDINAL STRESS-VOLUME RELATION

In a previous report we described the development of a Lagrangian analysis for combined compression and shear waves.[4] The analysis consists of solving the governing equations (Equations A.5 through A.8 in Appendix A) from a knowledge of $u_1(t)$ and $u_2(t)$ profiles at several locations. It has been shown previously that the longitudinal stress-volume (σ_x-V) relation is completely determined by the $u_1(t)$ profiles. This is true whether we have biwaves or uniaxial strain waves. The main advantage of the Lagrangian analysis is that the data are cast in a form that is easier to use for developing constitutive models. The results of an analysis of the $u_1(t)$ profiles are given below.

The uniaxial strain profiles from experiment 4 (78-2-25) were analyzed to give the stress-volume loading and unloading path shown in Figure 15. An elastic loading to 1 kbar can be observed. A peak stress of 10.6 kbar indicates the Hugoniot state. The loading and unloading states, except for late time unloading, are nearly similar at all gage locations.

A similar analysis was performed for experiment 3 (78-2-27) to provide the longitudinal stress-volume data under compression and shear loading. The loading path and peak states from experiments 3 and 4 are plotted with the LLL data in Figure 16. The broken line is the

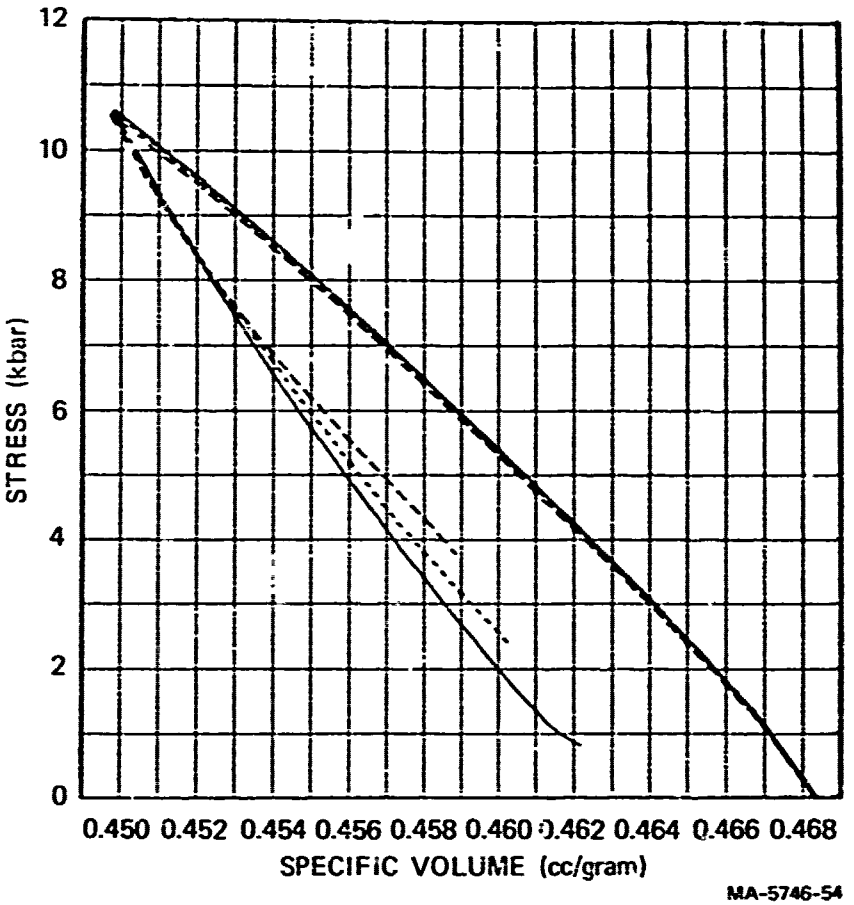

FIGURE 15 LONGITUDINAL STRESS-VOLUME LOADING AND UNLOADING PATH (EXPERIMENT 1, 78-2-25, UNAXIAL STRAIN)

All three gages follow nearly similar loading-unloading paths.

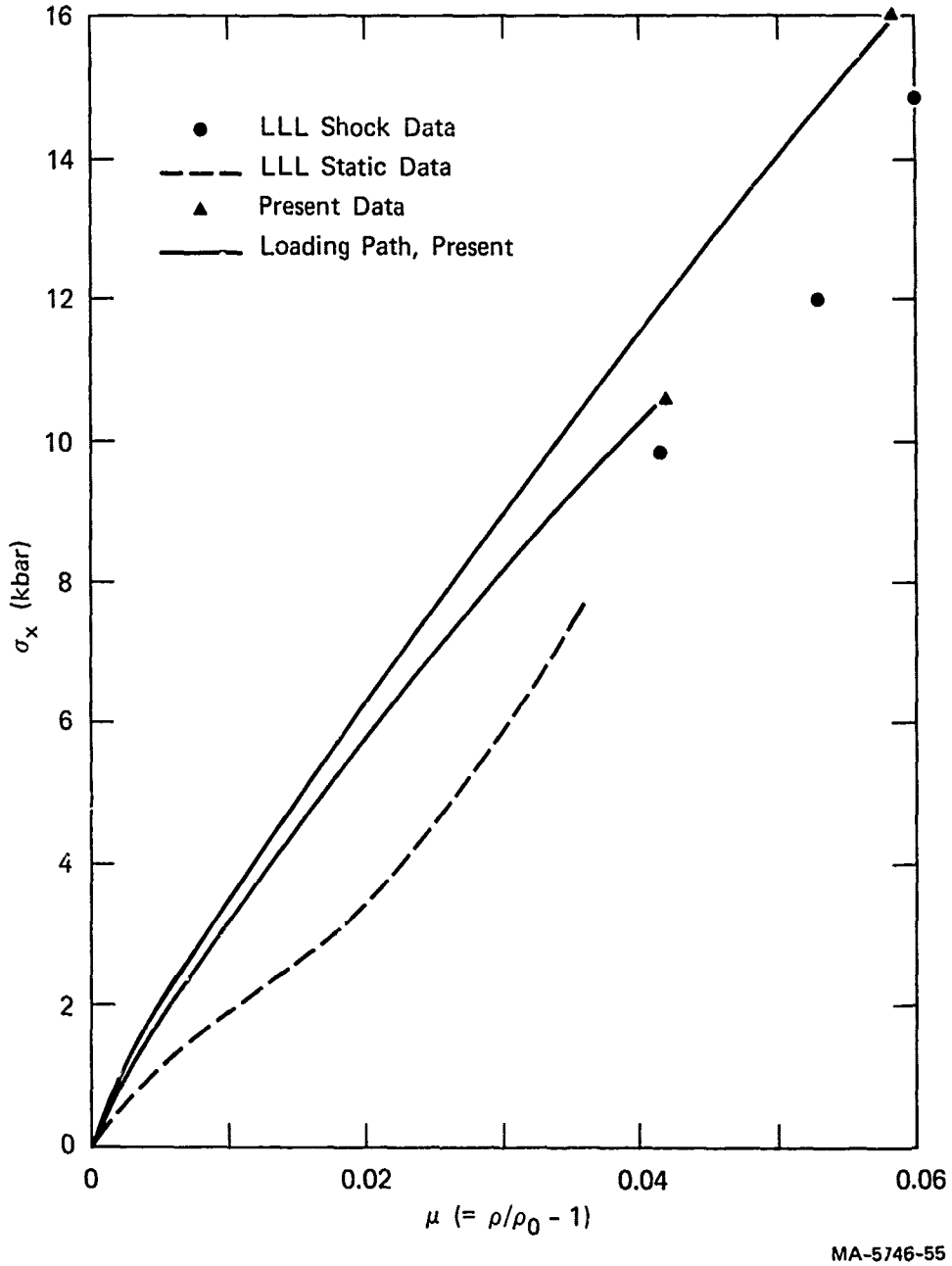

FIGURE 16 LONGITUDINAL STRESS AS A FUNCTION OF COMPRESSION ($\mu = \rho/\rho_0 - 1$)

LLL static uniaxial strain data,[5] and the circle points are the LLL Hugoniot data.[6] The LLL Hugoniot data indicate a more compliant material response than our data. We believe that this discrepancy is caused by differences in the material in our work and the LLL dynamic work. The density and longitudinal sound speed, reported by Anderson and Larson,[6] are smaller by 0.5% and 5%, respectively. Although all the differences are close to experimental accuracy limits, the consistently lower values for each case indicate that these differences are real. Our density and sound speed measurements are close to the LLL static work.

The main result inferred from Figure 16 is that the initial loading modulus is higher for the dynamic data than for the static data. At higher compressions, however, an extrapolation of the static data agrees with the final states observed in our work. The higher loading modulus at lower stresses is a consequence of rate-dependent pore-collapse; that is, for a given stress, less pore-compaction is observed at high rates than at low rates.

NUMERICAL CALCULATIONS OF WAVE PROFILES

To assess the constitutive model for salt presented in Section 3 and to extend it for handling dynamic material response, we made numerical simulations of the observed wave profiles, using the wave propagation program, COPS.[15,16] The COPS code was developed to study one-dimensional compression and shear wave propagation in solids. It is an extension of the one-dimensional codes used for studying uniaxial strain waves.[14] The impacting solids are modeled as planar slabs, and the governing equations are solved using the artificial viscosity method pioneered by von Numann and Richtmeyer.[17] To handle shear wave propagation, the code must also: (1) incorporate material rotation and consistent use of stress and strain measures, (2) use artificial viscosity for shear waves, (3) minimize the dispersion in the shear wave caused by the artificial viscosity and (4) properly specify the shear particle velocity at the impact surface.

The material model parameters, derived from the static parameters, were presented in Section 3. Adaptation of the model to the dynamic

calculations requires the specification of a relaxation time in the deviator stress model as indicated in Section 3 and a slightly stiffer P-V relation.* Both of these changes were incorporated by simulating the LLL uniaxial strain experiment having a peak particle velocity of 0.138 mm/μs (experiment NN-6 in reference 6). The values for the relaxation time T_r and the dynamic parameters for the P-V relation are listed in Table 4. All the simulations presented below were made with the same parameters.

Table 4

DYNAMIC PARAMETERS

T_r	0.05 μsec
P_1 = 0 kbar	V_1 = 0.4675 cm^3/g
P_2 = 0.5 kbar*	V_2 = 0.4663* cm^3/g
P_3 = 2.8 kbar*	V_3 = 0.4605 cm^3/g
P_4 = 5.7 kbar	V_4 = 0.4535 cm^3/g
DP_1 = 0 kbar*	
DP_2 = 0.12 kbar	
DP_3 = -0.3 kbar	

*These are the values that are different from the corresponding values shown in Table 3.

Figure 17(a) compares the numerically calculated wave profiles with the experimental data from LLL experiment NN-6. The agreement is quite good except that the calculated plastic wave is slightly stiffer. The irregular profile in gage 2 is an experimental artifact (either in

*In our work the dynamic relation was chosen by matching the wave arrival in experiment NN-6 of reference 6.

measurement or in data reduction) and was not observed in any other record.

Figure 17(b) shows the comparison for a higher stress experiment (NN-7 in reference 6). Good agreement is again observed between the experimental data and calculations. The slight increase in the particle velocity data at late time is an experimental artifact caused by lead stretching. In this comparison, the experimental profiles are steeper.

These two simulations show that the model presented here adequately fits the shock data obtained on salt. Using the same model, we simulated the combined compression and shear wave experiments in a similar manner. Particle velocities measured at the impact surface during experiments 3 and 4 (Section 2) were prescribed* and wave profiles were obtained at distances comparable to the gage locations. To minimize shear wave dispersion caused by artificial viscosity, we selected the lowest-allowable value of artificial viscosity.

Figure 18(a) compares the experimentally measured longitudinal profiles with the calculated wave profiles. Except for the steepness near the top of the plastic wave, the agreement is quite good. The numerically calculated and experimentally measured shear wave profiles are shown in Figure 18(b). The calculated wave profiles show wave arrival with an elastic shear wave speed followed by a very gradual increase in particle velocity. The peak amplitudes are much smaller than the prescribed particle velocity amplitude; that is, the shear wave amplitude is rapidly attenuated near the impact surface. This result is qualitatively similar to experimental observations. However, the arrival time and the structure in the shear wave data are very different from the calculated profiles. It is quite certain that the faster traveling longitudinal wave produces a voltage signal because of experimental artifacts (Section 2), but the exact magnitude of this signal is not easily known and cannot be easily subtracted from the

*In these simulations we need to simultaneously prescribe $u_1(t)$ and $u_2(t)$ at the impact surface.

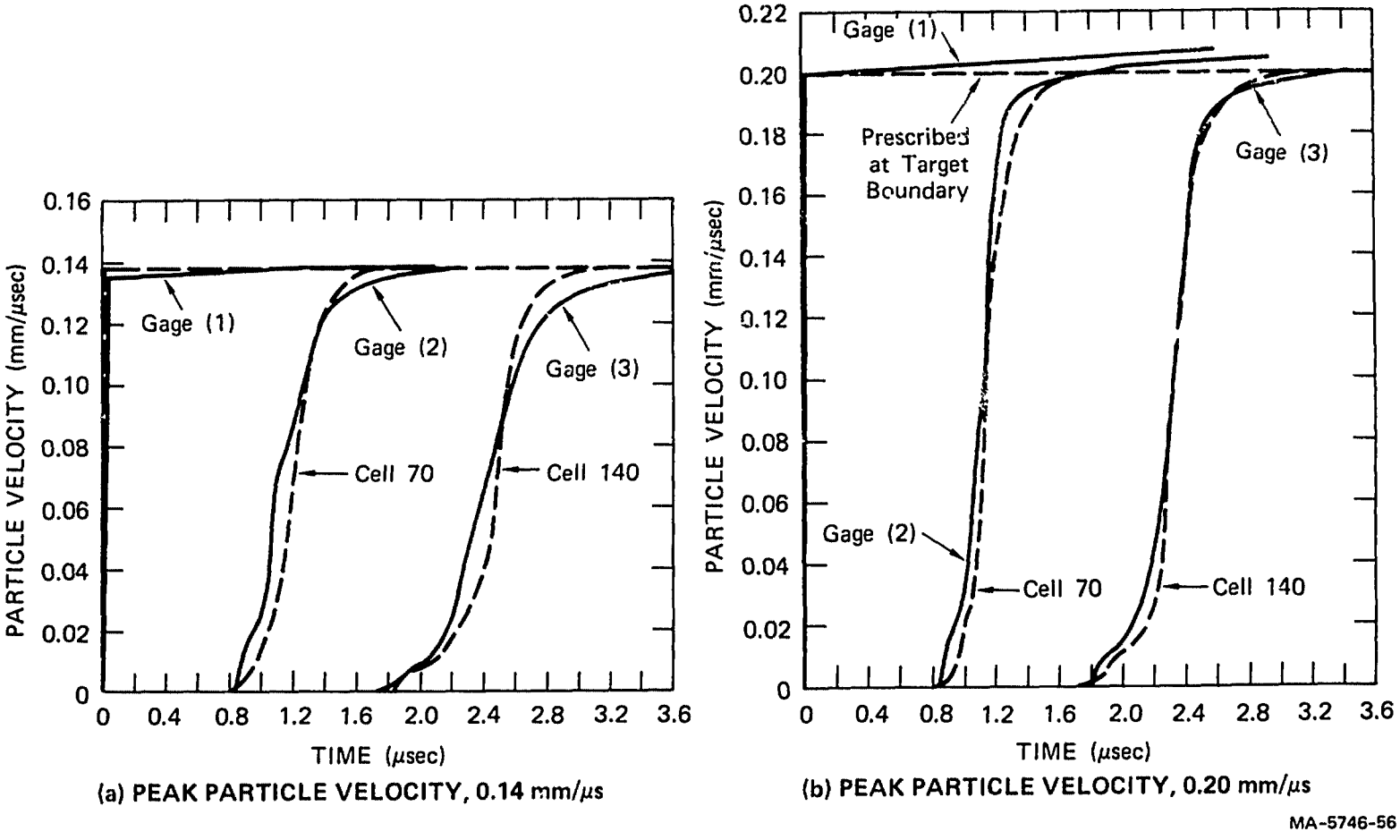

FIGURE 17 COMPARISON OF MODEL CALCULATIONS AND EXPERIMENTALLY MEASURED UNAXIAL STRAIN WAVE PROFILES

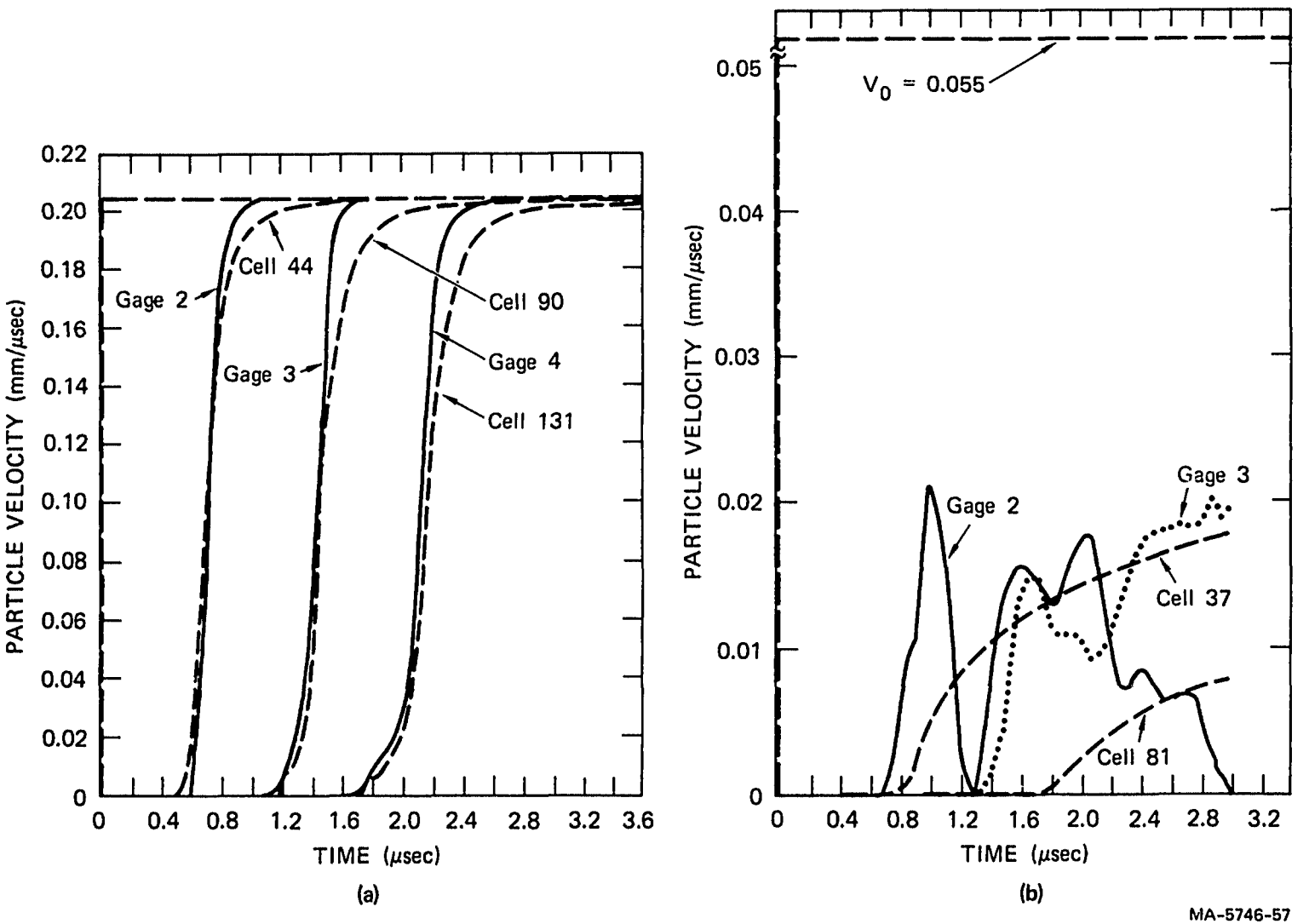

FIGURE 18 COMPARISON OF MODEL CALCULATIONS AND EXPERIMENTALLY MEASURED COMPRESSION AND SHEAR WAVE PROFILES

observed data. If, in Figure 18(b), we subtract the particle velocity amplitude in the experimental data at times corresponding to 0.8 μs* and 1.8 μs* from the late time amplitude, the remaining amplitude values are comparable to the calculated amplitudes. Unfortunately, there is little justification for this procedure.

The compression and shear wave simulations show that the constitutive model predicts the longitudinal wave profiles reasonably well. The calculated shear wave profiles show rapid attenuation with propagation distance, and the calculated amplitudes are small in accordance with experimental data. However, the arrival time and structure of the observed profiles are quite different from the calculated profiles. The probable causes of this discrepancy are experimental artifacts; it is not possible to use the shear wave data for an improvement of the material model outlined in Section 3.

LOCALIZATION OF THE SHEAR WAVE

The shear wave data on salt showed extremely rapid attenuation near the impact surface and very little shear motion coupled to the specimen interior. A similar result was also obtained from the numerical calculations. This rapid shear wave attenuation with propagation distance can be explained by a simple wave analysis as shown below.

The equations describing shear wave propagation can be written as (see Appendix A and reference 4)

$$\rho_o \frac{\partial u_2}{\partial t} = \frac{\partial \tau}{\partial h} \tag{20}$$

$$\frac{\partial \gamma}{\partial t} = \frac{1}{2}\frac{\partial u_2}{\partial h} \tag{21}$$

*These are times corresponding to the arrival of the shear waves in the calculations.

where we have written $h = X_1$, $\gamma = E_{12}$ $(= E_{21})$, and $\tau = T_{12}$ for convenience of typing. We now define a velocity

$$C_\alpha = \left(\frac{\partial h}{\partial t}\right)_\alpha \tag{22}$$

where the symbol α denotes either τ, γ, or u_2. Hence, C_α represents a velocity associated with a particular α value of the wave. Definition (22) is identical to the contour velocities introduced by Fowles in the analysis of uniaxial strain waves.[18]

Recognizing that u_2 is a function of the independent variables h and t we can derive*

$$C_{u_2} = \frac{-\left(\partial u_2/\partial t\right)_h}{\left(\partial u_2/\partial h\right)_t} \tag{23}$$

Combining Equations (21) and (23), we can express the change in γ at a gage location as

$$d\gamma = -\frac{du_2}{2C_{u_2}} \quad \text{along } h = \text{constant} \tag{24}$$

Knowledge of C_{u_2} as a function of u_2 enables us to integrate Equation (24) and determine $\gamma(t)$. An interesting aspect of Equation (24) pertinent to the present work concerns the relative magnitudes of du_2 and C_{u_2}. For $du_2 \gg 2C_{u_2}$, a very large increment in strain, $d\gamma$, is obtained. Unlike the compression wave, this inequality is very plausible for the shear wave. The consequences of this result are explored next.

---

* $u_2 = u_2\,(h,t)$

$$du_2 = \left(\frac{\partial u_2}{\partial h}\right) dh + \left(\frac{\partial u_2}{\partial t}\right) dt$$

For constant u_2 we get equation (23).

Defining C_τ similar to C_{u_2} and combining with Equations (20), (21), and (23), we can write

$$\frac{d\tau}{d\gamma} = 2\rho_o \, C_{u_2} C_\tau \text{ along } h = \text{constant} \tag{25}$$

Equation (25) expresses the modulus or the slope of the shear stress-strain relation at a gage location. Knowledge of C_{u_2} and C_τ over the h-t domain of an experiment can be used to obtain the dynamic τ-γ relation. A different but related procedure is used in the Lagrangian analysis presented in reference 4.

Equations (24) and (25) are applicable in general. To derive the relationship we seek, we will make some simplifying assumptions about the material. If we assume that $\tau = \tau(\gamma)$ and that wave propagation is into a constant region, as is generally the case, we can write[18]

$$C_{u_2} = C_\tau \tag{26}$$

Equation (26) can be combined with Equations (25) and (24) to give

$$C_{u_2} = \sqrt{\frac{1}{2\rho_o}\left(\frac{\partial \tau}{\partial \gamma}\right)_h} \tag{27}$$

and

$$d\gamma = -\frac{du_2}{2\sqrt{\frac{1}{2\rho_o}\left(\frac{\partial \tau}{\partial \gamma}\right)_h}} \tag{28}$$

Equation (28) shows that $d\gamma$ is determined by the relative magnitudes of du_2 and the shear stress-strain modulus. That is, large strains can build up (also termed 'localization') on the microsecond time scale even if C_{u_2} is significantly positive. Because this localization is controlled in part by the imposed motion, we refer to it as 'kinematic localization'.

Unlike compressive deformation, large shear strains inhibit propagation of large amplitude shear waves. This happens because large

shear strain results in rupture (resulting in stress drop) or a flattening of the shear stress-strain curve. The second effect occurs in our calculations, with the shear wave being localized near the impact surface. A similar localization is generally not observed in compressive wave propagation because the loading curve σ_x-V is concave upwards due to the curvature in the pressure-volume relation.

CONCLUSIONS

The objectives of the present work were to obtain the compression and shear wave profiles in salt and to interpret these data in terms of a constitutive model. These objectives have largely been met except for determining the precise cause of the observed structure in the shear wave profiles. With further effort, these causes could probably be determined and mitigated. The benefits of such an effort, from a practical viewpoint, are not obvious. The reasonable agreement between the simple constitutive model developed here and the experimental profiles suggests that similar modeling on natural salt is warranted. Furthermore, emphasis should be placed on accurate determination and modeling of the unloading portion of the longtitudinal profiles.

The granite results, though from a single experiment, suggest several areas of investigation in hard rocks. It would be interesting to determine if the amplitude of the shear wave that can be propagated into the material is related to the amplitude of the compression wave. The answer to this question depends on two competing effects and is not obvious. Increasing σ_1 increases both the mean stress and stress deviators. The increase in mean stress favors a larger amplitude shear wave, whereas an increase in stress deviator favors a reduction in the shear amplitude.

Because the shear wave propagates into a nearly constant region in the granite, the method developed by Gupta et al.[19] can be used to determine the dynamic mean stress-volume ($\sigma_{mm}/3$ versus V/V_o) relation. In this method a bulk modulus-density (K-ρ) relation is determined from experimental measurements of longitudinal and shear wave speeds in the

shocked state. The K-ρ curve is integrated to obtain the σ_{mm}-ρ/ρ_o relation. The knowledge of mean stress-volume relation permits a determination of the dynamic strength from existing uniaxial strain data. It would be desirable to determine if the material loses strength (under uniaxial strain) beyond a threshold compressive stress. In PMMA the dynamic material strength decreased beyond a threshold stress giving opposite results under dynamic and static uniaxial strain experiments.[19]

Finally, wave propagation across faults and joints is of interest to underground testing. An important question in these studies concerns the magnitude of dynamic friction and post-sliding behavior. While phenomenology experiments at small scale are useful, the inclined impact experiments can provide the quantitative data needed for material modeling. It would be useful to quantify the frictional behavior across interfaces in the presence of inelastic deformation because present knowledge in this area is quite limited. A direct measure of the frictional behavior at an interface is determined from the shear particle velocities across an interface.

REFERENCES

1. J. T. Cherry et al., "The Teleseismic Radiation Field From Explosions: Dependence of Seismic Amplitudes Upon Properties of Materials in the Source Region," Systems, Science and Software, La Jolla, Calif., Final Report, DNA 3113Z (1973).

2. T. C. Bache et al., "An Explanation of the Relative Amplitude of The Teleseismic Waves Generated by Explosions in Different Test Areas at NTS," Systems, Science and Software, La Jolla, Calif., Final Report, DNA 3958F (1975).

3. Y. M. Gupta, "Shear Wave Measurements in Shock Loaded Solids," Appl. Phys. Letters, 29, 694 (1976).

4. Y. M. Gupta, "Development of a Method for Determining Dynamic Shear Properties," SRI International, Menlo Park, Calif., Draft Final Report Submitted to the Defense Nuclear Agency (1978).

5. H. C. Heard et al., "Stress Strain Behavior of Poylcrystalline NaCl to 3.2 GPa," Lawrence Livermore Laboratory, Livermore, Calif., Report No. UCRL-51743 (1975).

6. G. D. Anderson and D. B. Larson, "Plane Shock Wave Studies of Geologic Media," Lawrence Livermore Laboratory, Livermore, Calif., Report No. UCRL-52357 (1977), see pages 12 and 13.

7. R. J. Christensen et al., "Torsional Shear Measurements of the Frictional Properties of Westerly Granite," Terra-Tek, Salt Lake City, Utah, Final Report, DNA 3359F (1977).

8. F. F. Voronov et al., "Effect of Pressures up to 20 kbars on the Elastic Characteristies of Sodium and Cesium Chlorides," Soviet Physics-Solid State, 13, 1131 (1971).

9. L. Seaman et al., "Computational Representation of Constitutive Relations for Porous Material," SRI International, Menlo Park, Calif., Final Report DNA 3412F (1974).

10. D. L. Decker, "Equation of State of Sodium Chloride," J. Appl. Phys., 37, 5012 (1966).

11. G. Simmons and H. Wang, Single Crystal Elastic Constants and Calculated Aggregate Properties: A Handbook (The MIT Press, Cambridge, Massachusetts, 1971).

12. Y. C. Fung, Foundations of Solid Mechanics (Prentice-Hall, Inc., New Jersey, 1965).

13. P. Perzyna, "Fundamental Problems in Viscoplasticity," in Advances in Applied Mechanics, (Academic Press, New York, 1966).

14. L. Seaman, "SRI PUFF 8 Computer Program for One-Dimensional Stress Wave Propagation," SRI International, Menlo Park, Calif., Draft Final Report to U.S. Army Ballistics Research Laboratory under Contract DAAK11-77-C-0083 (1978), page 177.

15. J. N. Johnson, "Dynamic Anisotropic Constitutive Relations for Oil Shale," Terra Tek, Salt Lake City, Utah, Report TR 75-25 (1975).

16. Y. M. Gupta, "COPS: Computer Program for Calculations of One-Dimensional P and S Waves in Solids" (unpublished).

17. J. von Neumann and R. D. Richtmyer, "A Method for the Numerical Calculation of Hydrodynamic Shocks," J. Appl. Phys., 21, 232 (1950).

18. G. R. Fowles, "Shock Wave Physics," in Metallurgical Effects at High Strain Rates (Plenum Press, New York-London, 1973)

19. Y. M. Gupta et al., "One-Dimensional Compression and Shear Wave Propagation in Polymethyl Methacrylate (PMMA)," Bull. Am. Phys. Soc. 24, 716 (1979).

Appendix A

COMPRESSION AND SHEAR WAVES IN IMPACTED SOLIDS

This appendix summarizes the IMPS* method for compression and shear wave measurements and presents the appropriate governing equations for describing wave propagation. An error analysis for shear particle velocity measurements is also presented.

EXPERIMENTAL MEASUREMENTS

The experimental method is based on the measurement of particle velocities, using Faraday's law for moving circuits, in the inclined plate impact experiment shown in Figure A.1. A flyer plate with velocity along the X_1'-axis impacts a parallel target plate. The normal to the impacting surfaces is along the X_1-axis. Upon impact, the target plate is imparted a motion having components along the X_1 and X_2 axes. By inserting thin metallic gages in the X_2-X_3 plane and measuring the EMF, ε, generated by their motion in a constant magnetic field, we can determine the particle velocities from the relation

$$\varepsilon = \vec{\ell} \cdot (\vec{u} \times \vec{B}) \qquad (A.1)$$

where $\vec{\ell}$ is the length vector for the gage, $\vec{u}$ is particle velocity, and $\vec{B}$ is the magnetic field. By measuring ε for two different $\vec{B}$ field orientations,† we can obtain the particle velocity time profiles $u_1(t)$ and $u_2(t)$. Improved accuracy is obtained by measuring either $u_1(t)$ or $u_2(t)$ profiles in a single experiment.‡

---

*Internal Measurements of P and S Waves.

†Except for the $\vec{B}$ fields, the experiments should be identical.

‡It has been shown elsewhere that experiments can be designed so that $u_1(t)$ and $u_2(t)$ can be measured simultaneously in a single experiment. However, this has not been done to date.

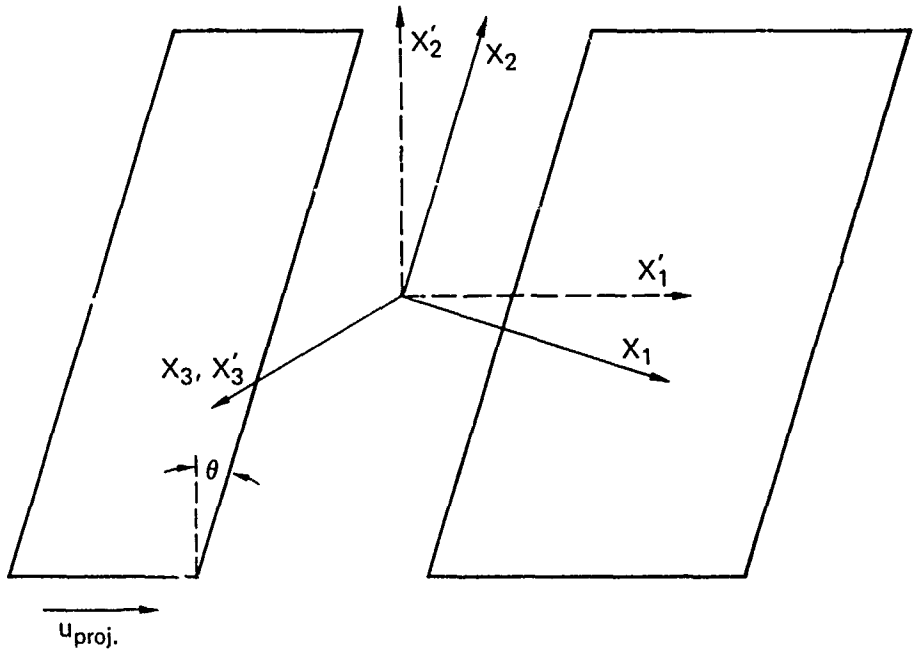

MA-5746-2C

FIGURE A.1 SCHEMATIC VIEW OF THE IMPACT OF TWO PARALLEL INCLINED PLATES

An experimental facility for impacting parallel inclined plates was designed and constructed under a previous DNA contract.* A magnet system was developed that provides the desired orientation of the $\vec{B}$ field in the X_1-X_2 plane. Target construction for these experiments is similar to the usual uniaxial strain experiment. In addition to the particle velocity profiles, each experiment measures impact velocity, tilt, and the magnetic field strengths. The errors in shear particle velocity measurements are discussed below.

Because the amplitude of the shear signal in the salt experiments was very small, it was important to establish the accuracy of this signal. To achieve this objective, we examined the magnitude of the signal that may be caused by the preceding longitudinal wave. Note that we are not considering any material effects such as coupling of longitudinal and shear motions due to nonlinear material response; instead, we are concerned only with experimental artifacts.

The particle velocity for the longitudinal wave is given by $\vec{u} = (u_1, 0, 0)$. For $\vec{B} = (B_1, 0, 0)$ and $\vec{\ell} = (\ell_1, \ell_2, \ell_3)$,† the longitudinal wave does not lead to a signal under ideal conditions (as determined from Equation A.1). However, all the above quantities can have small errors because of impact tilt, field misalignment, and gage placement.

We now estimate the error in the signal, $\Delta\varepsilon$, caused by experimental errors Δu, ΔB, and $\Delta\ell$ associated with the longitudinal wave. We will ignore terms of the order of Δ^2 because Δ itself is a very small quantity. We denote $\vec{u}$ and $\vec{B}$ as follows: $\vec{u} = (u_1, u_2, u_3)$ and $\vec{B} = (B_1, B_2, B_3)$. Here Δu_i (or ΔB_i) denotes the ith component of the small error in $\vec{u}$ or $\vec{B}$. We can then write

$$\Delta\varepsilon = \ell_2(B_1\,\Delta u_3 - u_1\,\Delta B_3) + \ell_3(u_1\,\Delta B_2 - B_1\,\Delta u_2) \qquad (A.2)$$

---

*Y. M. Gupta, "Development of a Method for Determining Dynamic Shear Properties," SRI International, Menlo Park, CA, Draft Final Report Submitted to the Defense Nuclear Agency (1978).

†The use of $\vec{\ell} = (\ell_1, \ell_2, \ell_3)$ considers the entire gage and not just the active element.

Figure A.2 shows the gage layout. To obtain $\Delta\varepsilon_{AD}$, we must evaluate Equation (A.2) for each of the three segments AB, BC, and CD. Each of these segments is supposed to be parallel to either the X_2 or X_3 axis, but it may have small deviations because of incorrect placement. However, the terms arising because of the incorrect placement are again of the order of Δ^2 and can be neglected. We can therefore write

$$\Delta\varepsilon_{AD} = (\ell_{AB} + \ell_{CD})(B_1\Delta u_3 - u_1\Delta B_3) + \ell_{BC}(u_1\Delta B_2 - B_1\Delta u_2) \qquad (A.3)$$

In Equation (A.3), ℓ_{AB} and ℓ_{CD} have opposite signs. Thus the first term on the right side of Equation (A.3) is again of the order of Δ^2 and is neglected. Hence,

$$\Delta\varepsilon_{AD} = \ell_{BC}\ (u_1\Delta B_2 - B_1\Delta u_2) \qquad (A.4)$$

Because the errors in u and B are independent, we need to add the two terms in the parenthesis. The error ΔB_2 is measured in each experiment. The error Δu_2 arises because of tilt and is estimated by determining the inclination of the wave front from tilt records.

Some typical values pertinent to Experiment 2 (78-2-33) described in Section 2 are

$$\ell_{BC} = 7.5 \text{ mm}$$
$$u_1 = 0.2 \text{ mm/}\mu\text{s}$$
$$B_1 = 3600 \text{ gauss}$$
$$\Delta B_2 = 50 \text{ gauss (for this particular shot)}$$
$$\Delta u_2 = 1.4 \times 10^{-3} \text{ mm/}\mu\text{s (taking the worst case)}$$

Using the above values we obtain $\Delta\varepsilon_{AD} \approx 11$ mV. This value of $\Delta\varepsilon_{AD}$ is equivalent to a Δu_2 value given by

$$\Delta u_2 \approx 2 \times 10^{-2}\ u_1 \qquad (A.5)$$

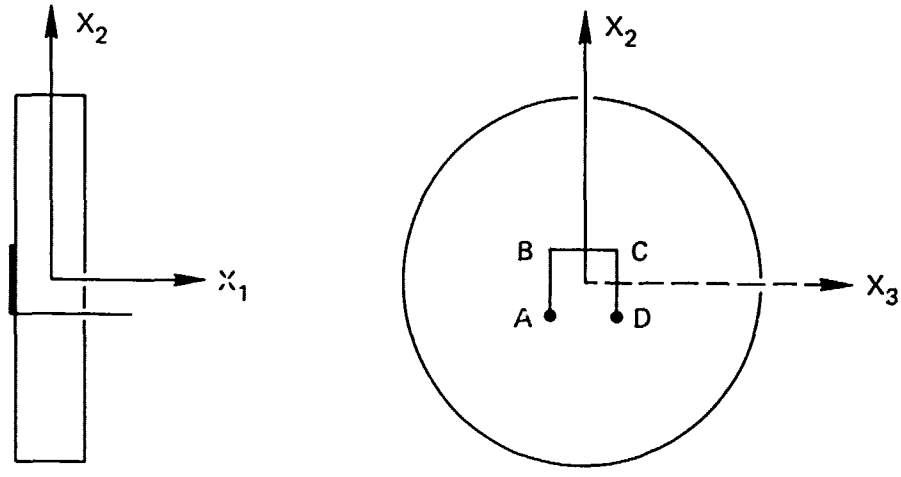

(a) SIDE VIEW

(b) FRONT VIEW

MA-5746-58

FIGURE A.2 GAGE LAYOUT

With more care, these errors can be reduced by a factor of 2 or 3. However, for the present experiments the value of u_2 in Equation (A.5) represents the accuracy limit of the shear wave amplitude in a combined compression and shear wave experiment.

GOVERNING EQUATIONS

In describing the wave propagation for the impact situation shown in Figure A.1, it is convenient to use the X_i-system. The governing equations are then one-dimensional; that is, variations with respect to only X_1 need to be considered. The current configuration, particle velocity, and deformation gradient are defined, respectively, as

$$x_i = x_i(X_m, t) \tag{A.6}$$

$$u_i = \left(\frac{\partial x_i}{\partial t}\right)_{X_m} \tag{A.7}$$

$$F_{ij} = \left(\frac{\partial x_i}{\partial X_j}\right)_t \tag{A.8}$$

With these definitions, we can write the equations governing wave propagation as

$$\rho_o\left(\frac{\partial u_i}{\partial t}\right) = \left(\frac{\partial T_{1i}}{\partial X_1}\right) \tag{A.9}$$

$$\rho_o\left(\frac{\partial V}{\partial t}\right) = \left(\frac{\partial u_1}{\partial X_1}\right) \tag{A.10}$$

$$\left(\frac{\partial E_{12}}{\partial t}\right) = 1/2\left(\frac{\partial u_2}{\partial X_1}\right) \tag{A.11}$$

$$\rho_o\left(\frac{\partial \varepsilon}{\partial t}\right) = T_{1i}\left(\frac{\partial u_i}{\partial X_1}\right) \tag{A.12}$$

where T_{1i} = First Piola-Kirchoff stress tensor

ρ_o = initial density

V = specific volume

$E_{ij} = \frac{1}{2}\left(\frac{\partial x_m}{\partial X_i}\frac{\partial x_m}{\partial X_j} - \delta_{ij}\right)$, a finite strain measure

ε = specific internal energy.

For the one-dimensional problem under consideration here, the stresses T_{11} and T_{12} are equal to the Cauchy stresses σ_{11} and σ_{12}. While σ_{12} is equal to σ_{21}, T_{12}, and T_{21} are not equal. The use of the symbol T in Equation (A.9) emphasizes this difference.

Appendix B

SUBROUTINE POROUS1--POROUS P-V MODEL

POROUS1 acts as a porous material P-V relationship. It consists of two sections: one section reads in the required data and initializes necessary parameters, and a second section computes the pressure corresponding to density increments determined by the wave propagation code. POROUS1 can be inserted into one-, two-, or three-dimensional codes.

Table B.1 is a glossary of the main variables used in POROUS1. A flow chart in Table B.2 outlines how the equations presented in Section 3 are used in the numerical calculations.

The argument list of POROUS1 is

```
SUBROUTINE POROUS1 (NCALL, IN, JCELL, M MATL, DI, EMG1,
                    EMG2, EMG3, EMG4, D, DOLD EINT, EOLD,
                    P, NCYC).
```

Most of these parameters are defined in Table B.1.

NCALL directs control to the data input and parameter initialization section or to the pressure computation section of POROUS1. POROUS1 data input and parameter initialization are performed as part of the problem-generating portion of the code. For example, SUBROUTINE SETUP is the primary problem-generating portion of the COPS code. Before the CALL to POROUS1, NCALL and IN are set equal to 0 and 5, respectively, indicating that control is to be transferred to the data input and parameter initialization section of POROUS1 and that the data are to be read in from input file 5. The CALL to POROUS1 in SETUP is

```
CALL POROUS1 (NCALL, IN, JE, M, MATL, RHO, EMG(1,M), EMG(2,M),
              EMG(3,M), EMG(4,M) T1, T2, T3, T4, T5).
```

The arguments T1 through T5 are nonessential for the input and initialization phase and are set = 0 before the CALL to POROUS1.

Table B.1

GLOSSARY OF MAIN VARIABLES IN POROUS1*

BKC (K_c)	-	Bulk modulus at consolidation
BKI (K_I)	-	Initial bulk modulus of porous material
BULK (K)	-	Linearly varying bulk modulus of porous material
D (ρ)	-	Current density
DC (ρ_c)	-	Consolidation density
DI (ρ_I)	-	Initial density of porous material
DIC (ρ_{so})	-	Density of nonporous material at ambient pressure
DOLD	-	Density at start of current solution step
EINT, EOLD	-	Current value of internal energy and value at start of current solution step, respectively; EOLD is not being used
EMG1, EMG2, EMG3, EMG4	-	Coefficients of Mie-Grüneisen equation for nonporous material (EMG1 = A, EMG2 = B in Equation 6)
ICON	-	Array of consolidation indicators for all the cells. ICON is 0 before consolidation and 1 after consolidation
JCELL	-	Cell number
M	-	Material number
MATL	-	Array that identifies material m
NPS	-	Number of parabolic segments defining porous P-V curve
P	-	Current pressure computed by POROUS1
PA	-	Pressure in the porous material during initial loading

*Items in parenthese represent the corresponding quantities using the notation of Section 3.

Table B.1 (concluded)

GLOSSARY OF MAIN VARIABLES IN POROUS1

PB	-	Pressure in the porous material during unloading or reloading
PMM (μ)	-	Measure of volumeric strain (D - DIC)/DIC
PORA, PORB, PORC	-	Coefficients (constant, linear, and quadratic terms, respectively) defining the parabolic segments of the porous P-V curve PORA = P_i PORB = $(P_{i+1} - P_i)/(V_{i+1} - V_i)$ PORC = $-4DP/(V_{i+1} - V_i)^2$
P1, P2 (P_i, P_{i+1})	-	Pressures at the endpoints of a parabolic segment
SPV	-	Array of specific volumes at the endpoints of the parabolic segments
V1, V2 (V_i, V_{i+1})	-	Specific volumes at the endpoints of a parabolic segment

Table B.2

FLOWCHART OF MAIN EQUATIONS IN POROUS1

(I) time = 0: READ in data and compute the coefficients of the parabolic segments defining the porous material P-V curve, i.e., for parabolic segment i, a, b, c in Equation (3) are given by

$$a = P_i,\ b = \frac{P_{i+1} - P_i}{V_{i+1} - V_i},\ c = \frac{-4DP}{(V_{i+1} - V_i)^2}$$

(II) time Δt:

(1) If material of cell j has consolidated (ICON(j) > 0 or D > DC), go to (7).

(2) Determine endpoint specific volumes bounding current specific volume.

(3) Compute pressure for initial loading

$P = a + b\ (V - V_i) + c\ (V - V_i)(V - V_{i+1})$ (from Equation 3)

(4) Compute current value for bulk modulus of porous material

$$K = K_I + \frac{K_c - K_I}{\rho_c - \rho_I}\ (\rho_{avg} - \rho_I)$$ (from Equation 5)

(5) Compute pressure for unloading or reloading of porous material

$P^n = P^{n-1} - K \cdot V/V_{avg}$ (from Equation 4)

(6) Actual pressure in porous material is given by the minimum of (3) and (5). Go to (8).

(7) Compute pressure for consolidated material,

$P = A\mu + B\mu^2$ (from Equation 6)

where $\mu = \rho/\rho_{so} - 1$

(8) RETURN.

The POROUS1 pressure computations occur during the solution portion of the code. For example, SUBROUTINE SWEEP is the routine in COPS that solves the governing equations (conservation of mass, momentum, and energy) to determine the particle velocities, displacement, and strains. It transfers control to the various material models to obtain stresses. Before the CALL to POROUS1, NCALL is set = 1, thus transferring control to the pressure computation portion of POROUS1.

A listing of POROUS1 is shown in Figure B.1.

```
SUBROUTINE  POROUS1                                  CDC 6700 FTN V3.0-355F OPT=1  79/06/29. 1

      SUBROUTINE POROUS1(NCALL,IN,JCELL,M,MATL,DI,EMG1,EMG2,EMG3,EMG4,
     1 D,DOLD,EINT,EOLD,P,NCYC)
C
C PEADS IN MATERIAL DATA AND COMPUTES PRESSURE FOR POROUS MATERIALS
C
C GLOSSARY OF VARIABLES IN ARGUMENT LIST
C       NCALL = 0 - READ MATERIAL DATA AND INITIALIZE
C       NCALL GT 0 - COMPUTE PRESSURE
C       IN - INPUT FILE I.D. ( NORMALLY IN = 5 )
C       JCELL - CELL NUMBER
C       M - MATERIAL NUMBER
C       MATL(I,M) - IDENTIFIES MATERIAL M
C       DI(M) - INITIAL DENSITY OF POROUS MATERIAL
C       EMG1-4 = COEFFICIENTS FOR MIE-GRUNEISEN EQ.
C       D - CURRENT DENSITY
C       DOLD - PREVIOUS DENSITY
C       EINT - CURRENT INTERNAL ENERGY
C       EOLD - PREVIOUS INTERNAL ENERGY
C       P - ENTERS AS THE PREVIOUS PRESSURE
C         - RETURNS AS THE CURRENT PRESSURE
C       NCYC - SOLUTION CYCLE NUMBER
C
C SOME OTHER VARIABLES
C
C       ICON(JCELL) = 0 - JCELL HAS NOT CONSOLIDATED
C                   = 1 - JCELL HAS CONSOLIDATED
C       DIC(M) - INITIAL DENSITY FOR HYDROSTAT
C       BKI(M) - INITIAL BULK MODULUS
C       BKC(M) - BULK MODULUS OF MATERIAL M AT CONSOLIDATION
C       NPS(M) - NO. OF PARABOLIC SEGMENTS
C       SPV(M,I) - SPECIFIC VOLUMES AT ENDPOINTS OF SEGMENTS
C       P1,P2 - PRESSURES AT BEGINNING AND END OF A SEGMENT
C       DELP - MAX PRESSURE DEVIATION ( FROM A LINEAR P - V
C              RELATIONSHIP ) FOR A PARABOLIC SEGMENT
C       PCRA(M,I),PCRB(M,I),PCRC(M,I) - COEFFICIENTS DEFINING A SEGMENT
C       DC(M) - DENSITY AT CONSOLIDATION
C       PA - PRESSURE IN POROUS MATERIAL AS PREDICTED FROM THE PARABOLIC
C       SEGMENTS
C       PB - PRESSURE IN POROUS MATERIAL PREDICTED FROM A PRESCRIBED
C            VARIATION OF THE BULK MODULUS ( BULK ) BETWEEN THE INITIAL
C            AND CONSOLIDATED STATES .
C
C DIMENSIONS ARE CURRENTLY SET FOR 4 MATERIALS WITH A MAX OF 5
C PARABOLIC SEGMENTS PER MATERIAL .
C
      DIMENSION MATL(4,1),DI(1)
      DIMENSION DIC(4),DC(4),BKI(4),BKC(4),NPS(4),SPV(4,5),
     1          PCRA(4,5),PCRB(4,5),PCRC(4,5),ICON(400)
C
      DATA NAT,NBT,NCT,NDT,NET
     1 /10H POROUS1 -,10H MATERIAL ,10H - GRM/CM3 ,10H - DYN/CM2,
     2  10H - CM3/GRM/
C
      IF(NCALL.GT.0) GO TO 2
C
```

FIGURE B.1 LISTING OF SUBROUTINE POROUS1

```
  SUBROUTINE   POROUS1                                    CDC 6700 FTN V3.0-359B OPT=1   79/06/29. 1
                C READ MATERIAL DATA
                C
                      READ(IN,1000) A2,DIC(M)
                1000 FORMAT(A10,E10.0)
60                    PRINT 9999
                9999 FORMAT( )
                      PRINT 2000,MAT,MAT,M,(MATL(I,M),I=1,4)
                2000 FORMAT(A10,A10,I5,3H - ,4A5/)
                      PRINT 2001,A2,DIC(M),NCT
65              2001 FORMAT(A10,E11.4,A10)
                      READ(IN,1001) A1,EMG1,A2,EMG2,A3,EMG3,A4,EMG4
                1001 FORMAT(4(A10,E10.0))
                      PRINT 2002, A1,EMG1,A2,EMG2,A3,EMG3,A4,EMG4
                2002 FORMAT(4(A10,E11.4)/)
70                    READ(IN,1003)A1,BK1(M),A2,BKC(M),A3,NPS(M)
                1003 FORMAT(2(A10,E10.3),A10,I5)
                      PRINT 2004,A1,BK1(M),A2,BKC(M),NCT,A3,NPS(M)
                2004 FORMAT(2(A10,F11.4),A10,A10,I5/)
                      READ(IN,1004)A1,(SPV(M,I),I=1,6)
75              1004 FORMAT(A10,6E10.0)
                      PRINT 2005,A1,(SPV(M,I),I=1,6),NCT
                2005 FORMAT(A10,6F11.5,A10/)
                C
                      NP=NPS(M)
80                    D1(M)=1./SPV(M,1)
                      DC(M)=1./SPV(M,NP+1)
                      P1=0.
                      DO 1 I=1,NP
                      READ(IN,1005)A1,P2,A2,DELP
85              1005 FORMAT(2(A10,E10.0,3))
                      PRINT 2006,A1,P2,A2,DELP,NDT
                2006 FORMAT(2(A1),E11.4),A10/)
                C
                C COMPUTE COEFFICIENTS DEFINING PARABOLIC SEGMENTS
                C
90                    DELV=SPV(M,I+1)-SPV(M,I)
                      PORA(M,I)=P1
                      PORB(M,I)=(P2-P1)/DELV
                      PORC(M,I)=-A.*DELP/(DELV*DELV)
95                  1 P1=P2
                      DO 2 I=1,400
                    2 ICON(I)=0
                      RETURN
                C
100             C PRESSURE CALCULATION
                C
                C DETERMINE APPROPRIATE DENSITY REGION. IF D GT DC, MATERIAL HAS
                C CONSOLIDATED AND THE PRESSURE IS COMPUTED USING THE MIE-GRUNEISEN EQ.
                C
105                 2 CONTINUE
                      IF(ICON(JCELL).GT.0) GO TO 5
                      NP=NPS(M)
                      IF(D.GT.DC(M)) GO TO 5
                C
110             C POROUS MATERIAL
```

FIGURE 6.1 LISTING OF SUBROUTINE POROUS1 (Continued)

```
      SUBROUTINE  POROUS1                                   CDC 6700 FTN V3.0-355R OPT=1  79/06/29. 1
C
      V=1./D
      VOLD=1./DOLD
      DO 3 J=1,NP
      JMAP=J+2
      K=J-1
      V1=SPV(M,K)
      V2=SPV(M,J)
      IF(V.GE.V2.AND.V.LE.V1) GO TO 4
    3 CONTINUE
      GO TO 7
    4 PA=PORA(M,K)+PORB(M,K)*(V-V1)+PORC(M,K)*(V-V1)*(V-V2)
C
C BULK IS THE AVERAGE OF THE BULK MODULI ASSOCIATED WITH THE CURRENT
C AND PREVIOUS DENSITIES OF THE POROUS MATERIAL.
C
      SLOPE=(BKC(M)-BKI(M))/(DC(M)-DI(M))
      DAVG=0.5*(D+DOLD)
      BULK=BKI(M)+SLOPE*(DAVG-DI(M))
      PBMP=BULK*(D-DOLD)/DAVG
      P=AMIN1(PA,PB)
C
      GO TO 9
C
C CONSOLIDATED MATERIAL
C
    5 ICON(JCELL)=1
C
C      PMU = DI*(1+MU)/(D1+D1C-D1)-1
C
C      WHERE MU = D/D1-1 = V1/V-1
C
      PMU=(C-D1C(M))/C1C(M)
      P=PMU*((EMG1+PMU*(EMG2+PMU*(EMG3)))*EMG4*ELSTOD
C
    9 CONTINUE
      RETURN
C
    7 PRINT 2007,NAT,MAT,M,V,SPV(M,1),NCYC
C
 2007 FORMAT(1H * * * ,A1),A1),15//40H  CURRENT SPECIFIC VOLUME,V =
     *E11.4/50H  HAS EXCEEDED INITIAL SPECIFIC VOLUME,SPV(M,1) =,E11.4/
     *15H  AT CYCLE NO. ,I5,27H, SOLUTION TERMINATED * * *)
      CALL EXIT
      END
```

FIGURE B.1 LISTING OF SUBROUTINE POROUS1 (Concluded)

Appendix C

DEVIATOR STRESS MODEL

The basic equations for the stress deviator model are presented in section 3. Here we derive the relations needed to use these equations in the numerical calculations. Listings of the stress deviator subroutine, VPSH, and the subroutine that describes the strain-hardening yield surface, J2I2P, are presented at the end of this appendix along with the procedure for inserting them into the wave propagation code (COPS).

ELASTIC STRESS-STRAIN RELATIONS

In the elastic region, an incremental form of Hooke's law is used to determine the stresses

$$d\sigma'_{ij} = 2G d\varepsilon'^{e}_{ij} \tag{C.1}$$

where

$$d\sigma'_{ij} \equiv d\sigma_{ij} - \frac{d\sigma_{mm}}{3}\,\delta_{ij}$$

$$d\varepsilon'_{ij} \equiv d\varepsilon_{ij} - \frac{d\varepsilon_{mm}}{3}\,\delta_{ij}$$

Here G is the shear modulus, assumed to be a function of pressure.

PLASTIC STRESS-STRAIN RELATIONS

A yield surface of the type

$$f(\sqrt{J'_2},\ \varepsilon'^{p}_{ij}) = 0 \tag{C.2}$$

is assumed to separate elastic and plastic deformations. In our model we assume plastic incompressibility and isotropic strain hardening. The yield surface consistent with these assumptions and the LLL data* is given by

$$f = Y_o + M(\sqrt{I_2'^p}) = 0 \qquad (C.3)$$

where Y_o = Yield stress expressed in terms of $\sqrt{J_2'}$

M = nonlinear strain-hardening coefficient

$$\sqrt{J_2'} = \sqrt{\frac{1}{2}\sigma_{ij}' \cdot \sigma_{ij}'}$$

$$\sqrt{I_2'^p} = \sqrt{\frac{1}{2}\varepsilon_{ij}'^p \cdot \varepsilon_{ij}'^p}$$

The function, f, was obtained from the uniaxial stress data obtained by Heard et al.* The strain-hardening plot ($\sqrt{J_{2E}'} - Y_o$ versus $\sqrt{I_2'^p}$ obtained from their data is shown in Figure C.1. This curve was fitted by a series of parabolic segments similar to those used in the porous pressure-volume relation (Section 3). The parameters describing these parabolic segments are given in Table C.1. The strain-hardening coefficient, M, for a particular strain increment can then be obtained from the secant modulus appropriately centered over the increment.

For a proportional loading experiment (like uniaxial stress), the plasticity model used here gives

$$\Delta\sqrt{I_2'^p} = \sqrt{\Delta I_2'^p} \qquad (C.4)$$

where $$\sqrt{\Delta I_2'^p} = \sqrt{\frac{1}{2}\Delta\varepsilon_{ij}'^p \cdot \Delta\varepsilon_{ij}'^p}$$

Equation (C.4), derived in the next subsection of this Appendix, is required for the strain-hardening model used here.

*H. C. Heard et al. "Stress Strain Behavior of Polycyrstalline NaCl to 3.2 GPa," Lawrence Livermore Laboraotry, Livermore, Calif., Report No. UCRL-51743 (1975).

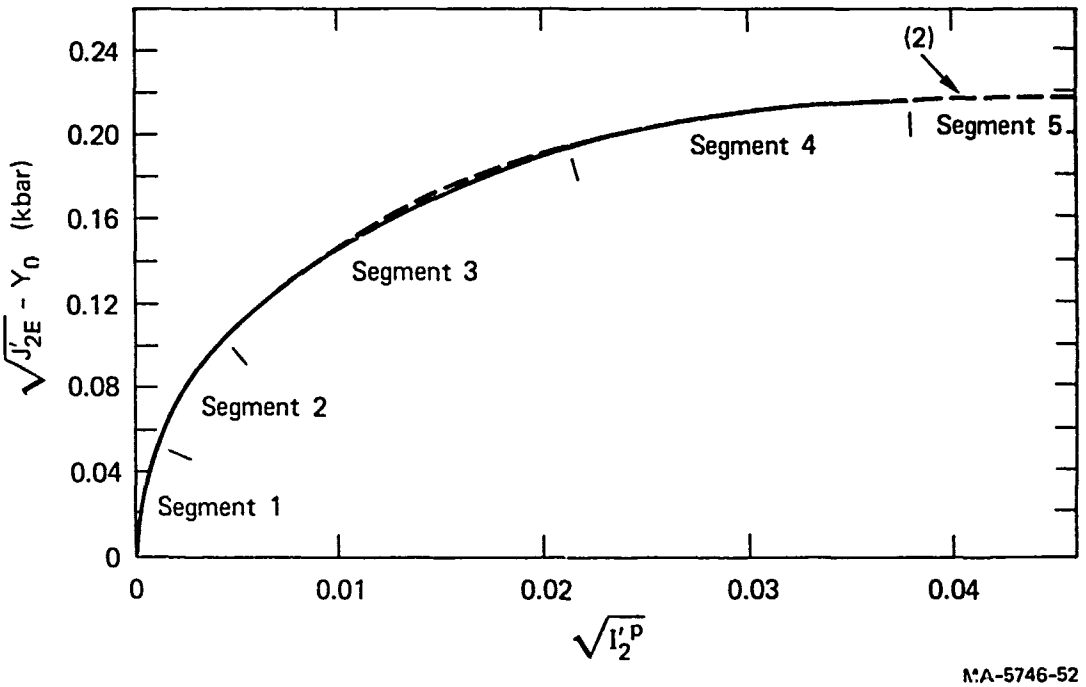

FIGURE C.1 STRAIN-HARDENING CURVE (SOLID LINE) OBTAINED FROM THE DATA OF HEARD ET AL.

The dotted line shown in segments 3 and 5 is the curve actually used.

Table C.1

PARAMETERS DEFINING THE SIX-SEGMENT PARABOLIC APPROXIMATION TO THE STRAIN-HARDENING CURVE

$\sqrt{J'_{2E}} - Y_o$ (kbar)	$\Delta[\sqrt{J'_{2E}} - Y_o]^*$ (kbar)	$\sqrt{I'^{P}_2}$
0.0	0.0	0.0
0.05197	0.007	0.000965
0.10393	0.01366	0.0042395
0.195		0.021223
	0.004	
0.218		0.037882
	0.0	
0.22		0.068
	0.0	
0.22		1.0

*$\Delta[\sqrt{J'_{2E}} - Y_o]$ is the maximum deviation from a linear $\sqrt{J'_{2E}} - Y_o$ versus $\sqrt{I'^{P}_2}$ variation.

At the start of a computational cycle, the deviatoric stresses are formed by assuming an elastic increment

$$\sigma'_{ijI} = \sigma'_{ijo} + 2G\Delta\varepsilon'_{ij} \tag{C.5}$$

where σ'_{ijo} = stress deviator at the end of previous computational cycle

G = current value of shear modulus

Equation (C.5) is used to compute $\sqrt{J'_{2I}}$. If $\sqrt{J'_{2I}}$ is not greater than the current yield strength $\sqrt{J'_{2E}}$ (or Y), no adjustment is made to the elastic stress values determined from (C.5), and the calculation proceeds. If $\sqrt{J'_{2I}}$ is outside the current yield surface, stresses are determined from the relation

$$\sigma'_{ij} = \sigma'_{ijI}\left[1 - \left(1 - \frac{\sqrt{J'_{2E}}}{\sqrt{J'_{2I}}}\right)\frac{\Delta t}{T_t}\right] \tag{C.6}$$

where T_R = relaxation time

Δt = time increment $\leq T_R$

For no strain-hardening, all quantities on the right side of (C.6) are known and σ_{ij} can be evaluated. Plastic strain increments are obtained from

$$\Delta\varepsilon'^{p}_{ij} = \frac{\sigma'_{ijI} - \sigma'_{ij}}{2G} = \frac{\sigma'_{ijI}}{2G}\left(1 - \frac{\sqrt{J'_2}}{\sqrt{J'_{2I}}}\right) \tag{C.7}$$

where $$\sigma'_{ij} = \sigma'_{ijI}\frac{\sqrt{J'_2}}{\sqrt{J'_{2I}}} \tag{C.8}$$

In the presence of strain-hardening, the value of $\sqrt{J'_{2E}}$ used in (C.6) must be consistent with the plastic strain generated during the increment. Strain hardening during a cycle is expressed as

$$\sqrt{J'_{2E}} = {}^{\circ}\sqrt{J'_{2E}} + M\sqrt{\Delta I'^{p}_{2}} \tag{C.8}$$

where ${}^{\circ}\sqrt{J'_{2E}}$ is the yield strength at the start of the current increment and M is the current work hardening modulus.* Using (C.7), we can write

$$\sqrt{\Delta I'^{p}_{2}} = \frac{\sqrt{J'_{2I}} - \sqrt{J'_{2}}}{2G} \tag{C.9}$$

Equation (C.6) can be expressed as

$$\sqrt{J'_{2}} = \sqrt{J'_{2I}}\left(1 - \frac{\Delta t}{T_R}\right) + \sqrt{J'_{2E}} \cdot \frac{\Delta t}{T_R} \tag{C.10}$$

Equations (C.8) through (C.10) have three unknowns, $\sqrt{\Delta I'^{p}_{2}}$, $\sqrt{J'_{2E}}$, and $\sqrt{J'_{2}}$. Hence a simultaneous solution can be obtained to give

$$\sqrt{\Delta I'^{p}_{2}} = \frac{\sqrt{J'_{2I}} - {}^{\circ}\sqrt{J'_{2E}}}{M + \dfrac{2GT_R}{\Delta t}} \tag{C.11}$$

Substituting (C.11) in (C.8), we get $\sqrt{J'_{2E}}$. This value when substituted in (C.6) gives σ'_{ij}. The plastic strain increment $\Delta\varepsilon'^{p}_{ij}$ can then be determined from Equation (C.7), and the calculation proceeds.

The simultaneous solution presented here is possible because of Equations (C.4) and (C.8) and the determination of M from Figure C.1. The last two items are discussed here and the derivation of Equation (C.4) is given in the next subsection of this appendix.

*M is a nonlinear function of $\sqrt{I'^{p}_{2}}$.

Equation (C.8) represents a linear work-hardening relation over the strain increment. This linear relationship is justified because we are using the current value of M, because strain hardening is monotonically increasing, and because we are using an incremental approach.

The determination of M from Figure C.1 relies on Equation (C.4) and the approximation $\Delta\varepsilon'^{p}_{ij} \approx \Delta\varepsilon'_{ij}$. While it is possible to improve on this approximation by iterating on M using the value obtained from Equation (C.11), the difference in the results is insignificant because of the relative magnitudes of M and G in Equation (C.11).

DERIVATION OF EQUATION (C.4)

$$\Delta\sqrt{I'^{p}_2} = \Delta\left[\frac{1}{2}\,\varepsilon'^{p}_{ij}\cdot\varepsilon'^{p}_{ij}\right]^{1/2} = \Delta\left[\frac{1}{2}\int d\varepsilon'^{p}_{ij}\int d\varepsilon'^{p}_{ij}\right]^{1/2} \tag{C.12}$$

The material model considered here is equivalent to the Prandtl-Reuss relations, which give

$$d\varepsilon'^{p}_{ij} = \sigma'_{ij}\,d\lambda \tag{C.13}$$

where $d\lambda$ is a nonnegative sealar. Substituting (C.13) on the right side of (C.12), we have*

$$\Delta\sqrt{I'^{p}_2} = \Delta\left[\frac{1}{2}\int\sigma'_{ij}d\lambda\cdot\int\sigma'_{ij}d\lambda\right]^{1/2} \tag{C.14}$$

For proportional loading, we can write

$$\sigma'_{ij} = \beta_{ij}\bar{\sigma} \tag{C.15}$$

*Note, $d\varepsilon^{p}_{mm} = 0$.

where $\bar{\sigma} = \sqrt{\frac{1}{2}\,\sigma'_{ij} \cdot \sigma'_{ij}}$ and β_{ij} is a proportionality constant. By taking the dot product of (C.15) with itself, we can write

$$\sqrt{\frac{1}{2}\,\beta_{ij} \cdot \beta_{ij}} = 1 \tag{C.16}$$

Substituting (C.15) in (C.14), we can take out β_{ij} from the resulting integral. Using (C.16) we can write

$$\Delta\sqrt{I_2'^{p}} = \Delta\left[\int \bar{\sigma}\, d\lambda\right] \tag{C.17}$$

If $d(\bar{\sigma}d\lambda)$ is defined over the limits of integration, the right side of (C.17) is simply $\bar{\sigma}\, d\lambda$. Using the definition of $\bar{\sigma}$, we have

$$\Delta\sqrt{I_2'^{p}} = \bar{\sigma}d\lambda = \sqrt{\frac{1}{2}\,\sigma'_{ij}d\lambda \cdot \sigma'_{ij}\, d\lambda} \tag{C.18}$$

Using (C.13), we can write

$$\Delta\sqrt{I_2'^{p}} = \sqrt{\frac{1}{2}\,\Delta\varepsilon'^{\,p}_{ij} \cdot \Delta\varepsilon'^{\,p}_{ij}} = \sqrt{\Delta I_2'^{p}} \tag{C.19}$$

The equivalence shown in (C.19) is possible because of the proportional loading assumed in (C.15). While the compression and shear experiments are nonproportional loading, the work-hardening function is constructed from the static uniaxial stress experiment, which involves proportional loading.

VPSH AND J2I2P INSERTION PROCEDURE

VPSH is a two-dimensional visco plastic, strain-hardening model. J2I2P defnines the isotropic strain-hardening curve used by VPSH. Both subroutines consist of two section, a data input and parameter initialization section and a computation section.

The argument lists of VPSH and J2I2P are as follows:

SUBROUTINE VPSh (NCALL, IN, J, M, MATL, YO, Y1, Y2, GO, G1, G2, DT, SXXT, SYYT,SZZT, SXYT, EXP, EYP, EZP, EXYP, EX, EY, EZ, EXY, INDY, DBUG)

and

SUBROUTINE J2I2P (NCALL, K, J, M, WHMO, I2P, J2E, DBUG).

Most of these parameters are defined in Tables C.2 and C.3. Table C.4 outlines how the equations presented above and in Section 3 are used in the numerical calculations.

In both subroutines, NCALL directs control to either the data input and parameter initialization section or the computation section. For NCALL = 0, VPSH reads in the required data from input film IN (usually = 5) and CALLS J2I2P, which in turn reads in the data that it requires from input file K(= IN) and initializes the necessary parameters, i.e., the coefficients defining the parabolic segments that approximate the isotropic strain-hardening curve, and the initial work-hardening modulus. For NCALL = 1, VPSH computes the relaxed deviatoric stresses and plastic strain increments. In the process of doing so, VPSH CALLS J2I2P with values of $\sqrt{I_2'^P}$ to obtain corresponding values of $\sqrt{J_{2E}'}$.

VPSH and J2I2P data input and parameter initialization are performed as part of the problem-generating portion of the code (e.g., SUBROUTINE SETUP in the COPS code). Before the CALL to VPSH, NCALL and IN are set equal to 0 and 5, respectively, indicating that control is to be transferred to the data input and parameter initialization sections of VPSH and J2I2P. The CALL to VPSH in SETUP is

CALL VPSH (NCALL, IN, J, M, MATL, YO(M), Y1(M), Y2(M), GO(M), G1(M), G2(M), T1, T2, T3, T4, T5, T6, T7, T8, T9, T10, T11, T12, T13, T14, IDBUG).

The arguments T1 through T14 are nonessential for the input and initialization phase and are set equal to 0 before the CALL to VPSH.

The VPSH computations of deviatoric stresses and deviatoric plastic strain increments occur during the solution portion of the code (e.g., SUBROUTINE SWEEP in the COPS code). VPSH is called in the portion of SWEEP that treats the deviator stress material models. Before the CALL to VPSH, NCALL is set equal to 1, thus transferring control to the computation sections of VPSH and J2I2P.

Figure C.2 shows a listing for subroutine VPSH, and Figure C.3 shows a listing for J2I2P.

Table C.2

GLOSSARY OF MAIN VARIABLES IN VPSH*

DEV ($\frac{d\epsilon_{mm}}{3}$)	- Volumetric strain increment
DEX, DEY, DEZ, DEXY ($d\epsilon_x^{'p}$, $d\epsilon_y^{'p}$, $d\epsilon_z^{'p}$, $d\epsilon_{xy}^{'p}$)	- Plastic deviatoric strain increments
DI2P ($\sqrt{\Delta I_2^{'p}}$)	- Second invariant of the plastic deviatoric strain increments
DT (Δt)	- Current time step
EX, EY, EZ, EXY ($d\epsilon_x$, $d\epsilon_y$, $d\epsilon_z$, $d\epsilon_{xy}$)	- Total strain increments
EXP, EYP, EZP, EXYP ($\epsilon_x^{'p}$, $\epsilon_y^{'p}$, $\epsilon_{xy}^{'p}$)	- Plastic deviatoric strains
EXPP, EYPP, EXPP, EXYPP	- Temporary plastic deviatoric strains obtained by assuming that the deviatoric strain increments are all plastic
GO, G1	- Constant and linear shear modulu-coefficients
G2	- Two times the shear modulus
I2P ($\sqrt{I_2^{'p}}$)	- Second invariant of the plastic deviatoric strains
I2PP	- Second invariant of the temporary plastic deviatoric strains
I2PO ($\sqrt{I_2^{'p}}$)	- Second invariant of the plastic deviatoric strains at the start of the current cycle.

*Items in parentheses represent the corresponding quantities using the notation of Section 3 and this Appendix.

Table C.2 (continued)

GLOSSARY OF MAIN VARIABLES IN VPSH*

J2E ($\sqrt{J_{2E}'}$)	- Second invariant of the equilibrium deviatoric stresses (computed from Eq. C.8)
J2EA	- Second invariant of the equilibrium deviatoric stresses (corresponding to I2P)
J2EP	- Second invariant of the equilibrium deviatoric stresses corresponding to the temporary plastic deviatoric strains
J2EO ($^{o}\sqrt{J_{2E}'}$)	- Second invariant of the equilibrium deviatoric stresses at the start of the current cycle (corresponds to I2PO)
J2T ($\sqrt{J_{2I}'}$)	- Second invariant of the deviatoric stresses computed assuming all elastic strain increments
M	- Material number
MATL	- Array that identifies material m.
RELAXF $\left[1-\left(1-\frac{\sqrt{J_{2E}'}}{\sqrt{J_{2I}'}}\right)\frac{\Delta t}{T_r}\right]$	- Relaxation function
SXX, SYY, SZZ, SXY (σ_x', σ_y', σ_z', σ_{xy}')	- Relaxed deviatoric stresses

*Items in parentheses represent the corresponding quantities using the notation of Section 3 and this Appendix.

Table C.2 (concluded)

GLOSSARY OF MAIN VARIABLES IN VPSH*

SXXT, SYYT, SZZT, SXYT (σ'_{xI}, σ'_{yI}, σ'_{zI}, σ'_{xyI})	- Deviatoric stresses computed assuming all elastic strain increments
	- Set equal to SXX, SYY, SZZ and SXY before RETURN from VPSH
TAUO (T_r)	- Relaxation time constant
WHM (M)	- Work-hardening modulus
WHMO	- Work-hardening modulus at start of current cycle

*Items in parentheses represent the corresponding quantities using the notation of Section 3 and this Appendix.

Table C.3

GLOSSARY OF MAIN VARIABLES IN J2I2P*

C1, C2, C3	- Coefficients of constant, linear, and quadratic terms, respectively, of parabolic segments used to approximate the strain-hardening curve
$C1 = (\sqrt{J'_{2E}})_i$	
$C2 = [(\sqrt{J'_{2E}})_{i+1} - (\sqrt{J'_{2E}})_i]/[(\sqrt{I'^{p}_2})_{i+1} - (\sqrt{I'^{p}_2})_i]$	
$C3 = -4\Delta[\sqrt{J'_{2E}} - Y_o]_i/[(\sqrt{I'^{p}_2})_{i+1} - (\sqrt{I'^{p}_2})_i]^2$	
DY ($\Delta[\sqrt{J'_{2E}} - Y_o]_i$)	- Maximum deviation from a linear $(\sqrt{J'_{2E}} - Y_o)$ versus $\sqrt{I'^{p}_2}$ variation for segment i
I2P ($\sqrt{I'^{p}_2}$)	- Second invariant of the deviatoric plastic strain
J2E ($\sqrt{J'_{2E}}$)	- Second invariant of the equilibrium deviatoric stresses
	- Corresponds to I2P
M	- Material number
NPS	- Number of parabolic segments
WHMO	- Initial work-hardening modulus
X	- Array containing the endpoint values of $\sqrt{J'_{2E}} - Y_o$
Y	- Array containing the endpoint value of $\sqrt{I'^{p}_2}$
YO (Y_o)	- $\sqrt{J'_{2E}}$ at initial yield

*Items in parentheses represent the corresponding quantities using the notation of Section 3 and this appendix.

Table C.4

FLOWCHART OF MAIN EQUATIONS IN VPSH AND J2I2P

(I) time = 0: READ in data in VPSH, CALL J2I2P to READ in data and compute the coefficients of the parabolic segments defining the strain-hardening curve, i.e., for segment i, a, b, c in Eq. (3) are given by

$$a = (\sqrt{J'_{2E}})_i, \quad b = \frac{(\sqrt{J'_{2E}})_{i+1} - (\sqrt{J'_{2E}})_i}{(\sqrt{I'^{p}_2})_{i+1} - (\sqrt{I'^{p}_2})_i}, \quad c = \frac{-4\Delta[\sqrt{J'_{2E}} - Y_o]_i}{(\sqrt{I'^{p}_2})_{i+1} - (\sqrt{I'^{p}_2})_i)^2}$$

(II) time $\geq \Delta t$:

(1) Compute the trial deviatoric stresses*

$$\sigma'_{ijI} = \sigma'_{ijo} + 2G\,\Delta\,\varepsilon'_{ij} \tag{C.5}$$

(2) Form $\sqrt{J'_{2I}} = \sqrt{\frac{1}{2}\,\sigma'_{ijI}\,\sigma'_{ijI}}$

(3) If $\sqrt{J'_{2I}} \leq {}^{\circ}\sqrt{J_{2E}} \rightarrow \Delta\,\varepsilon'^{\,p}_{ij} = 0 \rightarrow$ go to (15)

(4) Form ${}^{\circ}\sqrt{I'^{p}_2} = \sqrt{\frac{1}{2}\,\varepsilon'^{\,p}_{ijo}\;\varepsilon'^{\,p}_{ijo}}$ (C.3)

(5) CALL J2I2P to obtain ${}^{\circ}\sqrt{J'_{2E}}$

(6) Compute the plastic deviatoric strains assuming the deviatoric strain increments are all plastic

$$\varepsilon'^{p}_{ij} = \varepsilon'^{\,p}_{ijo} + \Delta\varepsilon'_{ij}$$

(7) Form ${}^{*}\sqrt{I'^{p}_2} = \sqrt{\frac{1}{2}\,\varepsilon'^{p}_{ij}\,\varepsilon'^{p}_{ij}}$

*This is done in the COPS SUBROUTINE SWEEP.

Table C.4 (continued)

FLOWCHART OF MAIN EQUATIONS IN VPSH AND J2I2P

(8) CALL J2I2P to obtain $^{*}\sqrt{J'_{2E}}$

(9) Determine the work-hardening modulus

$$M = (^{*}\sqrt{J'_{2E}} - {}^{\circ}\sqrt{J'_{2E}})/(^{*}\sqrt{I'^{p}_{2}} - {}^{\circ}\sqrt{I'^{p}_{2}})$$

$$IF(^{*}\sqrt{I'^{p}_{2}} - {}^{\circ}\sqrt{I'^{p}_{2}}) \leq 0,\ M = {}^{\circ}M$$

(10) Compute

$$\sqrt{\Delta I'^{p}_{2}} = (\sqrt{J'_{2I}} - {}^{\circ}\sqrt{J'_{2E}})/(M + \frac{2GT_r}{\Delta t}) \qquad (C.11)$$

(11) Compute $\sqrt{J'_{2E}} = {}^{\circ}\sqrt{J'_{2E}} + M\sqrt{\Delta I'^{p}_{2}}$ (C.8)

(12) Form the relaxation function and compute the relaxed deviatoric stresses

$$\sigma'_{ij} = \sigma'_{ijI}\ \{1 - \left[1 - \frac{\sqrt{J'_{2E}}}{\sqrt{J'_{2I}}}\right]\frac{\Delta t}{T_r}\} \qquad (C.6)$$

(13) Compute the plastic deviatoric strain increments and update the plastic deviatoric strains,

$$\Delta\varepsilon'^{p}_{ij} = (\sigma'_{ijI} - \sigma'_{ij})/2G \qquad \text{(from Equation (15) and (C.7)}$$

$$\varepsilon'^{p}_{ij} = \varepsilon'^{p}_{ijo} + \Delta\varepsilon'^{p}_{ij}$$

*This is done in the COPS SUBROUTINE SWEEP.

Table C.4 (concluded)

FLOWCHART OF MAIN EQUATIONS IN VPSH AND J2I2P

(14) Update the work-hardening modulus for the next cycle

(14.a) Form $\sqrt{I_2'^p} = \sqrt{\frac{1}{2}\,\varepsilon_{ij}'^p\,\varepsilon_{ij}'^p}$

(14.b) CALL J2I2P to obtain $\sqrt{J_{2E}'}$

(14.c) $^{\circ}M = (\sqrt{J_{2E}'} - {}^{\circ}\sqrt{J_{2E}'})/(\sqrt{I_2'^p} - {}^{\circ}\sqrt{I_2'^p})$

If $(\sqrt{I_2'^p} - {}^{\circ}\sqrt{I_2'^p}) \leq 0$, $^{\circ}M$, = M from (9)

(15) RETURN

```
SUBROUTINE  VPSH                                    CDC 6700 FTN V3.0-355F OPT=1  79/06/29.
                      SUBROUTINE VPSH(NCALL,IN,J,M,MATL,Y0,Y1,Y2,G0,G1,G2,DT,SXXT,SYYT,
                     1 SZZT,SXYT,EXP,EYP,EZP,EXYP,EX,EY,EZ,EXY,INDY,DBUG)
                     C
                     C 2-D VISCO-PLASTIC WITH STRAIN HARDENING MATERIAL MODEL       5 - 74
                     C
                     C       NCALL = 0 - READ IN DATA AND INITIALIZE PARAMETERS
                     C             = 1 - COMPUTE DEV.STRESSES AND PLASTIC STRAIN INCREMENTS
                     C       IN = INPUT FILE ( USUALLY = 5 )
                     C       J = CELL NO.
                     C       M = MATERIAL NO.
                     C       MATL = ID OF MATERIAL M
                     C       Y0,Y1,Y2 = YIELD FUNCTION COEFFICIENTS
                     C       G0,G1 = SHEAR MODULUS FUNCTION COEFFICIENTS
                     C       G2 = 2*SHEAR MODULUS
                     C       DT = CURRENT TIME INCREMENT
                     C       SXXT,SYYT,SZZT,SXYT = TRIAL DEVIATORIC STRESSES ON INPUT,
                     C                           = RELAXED DEVIATORIC STRESSES ON OUTPUT
                     C       EXP,EYP,EZP,EXYP = DEV. PLASTIC STRAINS AT END OF PREVIOUS TIME
                     C                          STEP ON INPUT, CURRENT ON OUTPUT
                     C       EX,EY,EZ,EXY = CURRENT TOTAL STRAIN INCREMENTS
                     C       INDY = YIELD INDICATOR
                     C       DBUG = DEBUG INDICATOR
                     C
                           DIMENSION MATL(4,1),WHM0(4)
                           REAL J2T,I2P0,J2E0,I2PP,J2EP,J2E,I2P,J2EA
                           INTEGER DBUG
                           COMMON/TEMP/J2E0,J2EP,J2E,I2P0,I2PP,J2EA
                           IF(NCALL.GT.0) GO TO 10
                     C
                     C READ IN MATERIAL DATA AND INITIALIZE PARAMETERS
                     C
                           PRINT 1000,(MATL(I,M),I=1,4)
                      1000 FORMAT(//82H    * * * DATA FOR VISCO-PLASTIC WITH STRAIN HARDENING
                          1MATERIAL MODEL - MATERIAL = ,4A5,6H * * *)
                           READ(IN,100) A1,Y0,A2,Y1,A3,Y2
                       100 FORMAT(4(A1),E10.3))
                           PRINT 1001,A1,Y0,A2,Y1,A3,Y2
                      1001 FORMAT(4(A10,1PE10.3))
                           READ(IN,100) A1,G0,A2,G1
                           PRINT 1001,A1,G0,A2,G1
                           READ(IN,100) A1,TAU0
                           PRINT 1001,A1,TAU0
                           DUM1=DUM2=0.
                           CALL J2I2P(NCALL,IN,J,M,WHM0(M),DUM1,DUM2,DBUG)
                           RETURN
                     C
                     C COMPUTE DEVIATORIC STRESSES AND DEVIATORIC PLASTIC STRAIN INCREMENTS
                     C
                     C CHECK FOR YIELDING
                        10 J2T=SQRT(0.5*(SXXT**2+SYYT**2+SZZT**2)+SXYT**2)
                           I2P0=SQRT(0.5*(EXP**2+EYP**2+EZP**2)+EXYP**2)
                           CALL J2I2P(NCALL,IN,J,M,WHM0(M),I2P0,J2E0,DBUG)
                           IF(DBUG.EQ.1) PRINT 2000,SXXT,SYYT,SZZT,SXYT,EXP,EYP,EZP,EXYP,I2P0
                          1 ,J2E0,J2T
                      2000 FORMAT(*  VPSH(2000) - SXXT,SYYT,SZZT,SXYT =*,1P4E12.4/*  EXP,EYP,
```

FIGURE C.2 LISTING OF SUBROUTINE VPSH

```
      SUBROUTINE  VPSH                                        CDC 6700 FTN V3.0-355F OPT=1  79/06/29. 1
     1EZP,EXYP =*,4E12.4,* I2P0,J2E0,J2T =*,3E12.4)
           IF(J2T.LE.J2E0) GO TO 20
           INCY=1HP
     C COMPUTE THE PLASTIC DEV. STRAINS ASSUMING THE TOTAL DEV. STRAIN
     C INCREMENTS ARE ALL PLASTIC
           DEV=(EX+EY+EZ)/3.
           DEX=EX-DEV
           DEY=EY-DEV
           DEZ=-DEX-DEY
           DEXY=EXY
           EXPP=EXP+DEX
           EYPP=EYP+DEY
           EZPP=EZP+DEZ
           EXYPP=EXYP+DEXY
     C COMPUTE THE WORK HARDENING MODULUS
           I2PP=SQRT(0.5*(EXPP**2+EYPP**2+EZPP**2)+EXYPP**2)
           CALL J2I2P(NCALL,IN,J,M,WHM0(M),I2PP,J2EP,DBUG)
           WHM=WHM0(M)
           IF((I2PP-I2P0).GT.0.) WHM=(J2EP-J2E0)/(I2PP-I2P0)
           IF(DBUG.EQ.1) PRINT 2001,DEX,DEY,DEZ,DEXY,EXPP,EYPP,EZPP,EXYPP,
          1 I2PP,J2EP,WHM,WHM0(M),G2
      2001 FORMAT(*  VPSH(2001) - DEX,DEY,DEZ,DEXY =*,1P4E12.4/*  EXPP,EYPP,E
          1ZPP,EXYPP =*,4E12.4/*  I2PP,J2EP,WHM,,WHM0)(M),G2 =*,5E12.4)
     C COMPUTE THE INC. INV. OF THE PLASTIC DEV. STRAIN INCREMENTS.
     C THE EQUILIBRIUM VALUE OF J2, THE RELAXATION FUNCTION, AND THE RELAXED
     C DEV. STRESSES
     C                                                                    TD=DUAT
           D=(G2*TAU0/DT)+WHM
           D12P=(J2T-J2E0)/D
           J2E=J2E0+WHM*D12P
           RELAXF=1.-(1.-J2E/J2T)*DT/TAU0
           SXX=SXXT*RELAXF
           SYY=SYYT*RELAXF
           SZZ=-SXX-SYY
           SXY=SXYT*RELAXF
     C UPDATE THE PLASTIC DEV. STRAINS
           EXP=EXP+(SXXT-SXX)/G2
           EYP=EYP+(SYYT-SYY)/G2
           EZP=-EXP-EYP
           EXYP=EXYP+(SXYT-SXY)/G2
           IF((I2PP-I2P0).GT.0.) GO TO 11
           I2P=SQRT(0.5*(EXP**2+EYP**2+EZP**2)+EXYP**2)
           CALL J2I2P(NCALL,IN,J,M,WHM0(M),I2P,J2EA,DBUG)
           IF((I2P-I2P0).GT.0.) WHM0(M)=(J2EA-J2E0)/(I2P-I2P0)
           GO TO 12
        11 WHM0(M)=WHM
           J2EA=J2E
        12 CONTINUE
           IF(DBUG.EQ.1) PRINT 2002,D12P,J2E,I2P,J2EA,WHM0(M),RELAXF,SXX,SYY,
          1 SZZ,SXY,EXP,EYP,EZP,EXYP
      2002 FORMAT(*   VPSH(2002) - D12P,J2E,I2P,J2EA,WHM0(M),RELAXF =*,
          1 1P6E12.4/*     SXX,SYY,SZZ,SXY =*,4E12.4/*     EXP,EYP,EZP,EXYP =*,
          2 4E12.4)
           SXXT=SXX
           SYYT=SYY
```

FIGURE C.2 LISTING OF SUBROUTINE VPSH (Continued)

```
      SUBROUTINE   VPSH                                  CDC 6700 FTN V3.0-355F OPT=1   79/06/29.

                        SZZT=SZZ
                        SXYT=SXY
                        RETURN
                   20   INCY=1HE
  115                   RETURN
                        END
```


FIGURE C.2 LISTING OF SUBROUTINE VPSH (Concluded)

```
SUBROUTINE  J212P                                   CDC 6700 FTN V3.0-355P OPT=1  79/06/29. 1
                      SUBROUTINE J212P(NCALL,K,J,M,WHM0,I2P,J2E,DBUG)
                C
                C COMPUTES THE 2ND. INVARIANT OF THE DEVIATORIC SRESS TENSOR ( AT
                C EQUILIBRIUM ) ( J2E ) GIVEN THE CURRENT VALUE OF THE 2ND. INVARIANT OF
 5              C THE DEVIATORIC PLASTIC STRAIN TENSOR ( I2P ).
                C
                C USES PARABOLIC SEGMENTS WHICH ARE FIT TO A J2E-I2P CURVE BASED ON
                C MEASURED DATA.
                C
10              C      NCALL = 0 - READ IN DATA FOR MATERIAL M AND COMPUTE THE COEFFICIENTS
                C                  DEFINING THE NPS(M) PARABOLIC SEGMENTS
                C            # 1 - GIVEN I2P, COMPUTE J2E
                C      K = INPUT FILE ( USUALLY = 5 )
                C      J = CELL NO.
15              C      M = MATERIAL NO.
                C      WHM) = INITIAL WORK HARDENING MODULUS
                C      DBUG = DBUG PARAMETER
                C
                C ROUTINE IS CURRENTLY ( AS OF 5 - 79 ) DIMENSIONED FOR A MAX OF 4 MATERIALS
20              C AND 6 PARABOLIC SEGMENTS PER MATERIAL
                C
                      DIMENSION NPS(4),X(7),Y(7),DY(6),C1(4,6),C2(4,6),C3(4,6)
                      REAL I2P,J2E
                      INTEGER DBUG
25                    IF(NCALL.GT.0) GO TO 20
                C
                C READ IN DATA AND INITIALIZE PARAMETERS
                C
                      READ(K,100) A1,NPS(M),A2,A3,Y0
30                100 FORMAT(A1),I5,A1),A1),E1).3)
                      PRINT 1000,M,A1,NPS(M),A2,A3,Y0
                1000 FORMAT(//43H    * * * STRAIN HARDENING DATA FOR MATERIAL,I2/
                     1 A10,I5,A10,A10,1PE12.4)
                      N=NPS(M)
35                    N1=N+1
                      READ(K,200) A1,(X(I),I=1,N1)
                 200 FORMAT(A10,7E10.0)
                      PRINT 2000,A1,(X(I),I=1,N1)
                2000 FORMAT(A10,1P7E12.4)
40                    READ(K,200) A1,(Y(I),I=1,N1)
                      PRINT 2000,A1,(Y(I),I=1,N1)
                      READ(K,200) A1,(DY(I),I=1,N)
                      PRINT 2000,A1,(DY(I),I=1,N)
                C COMPUTES THE COEFFICIENTS DEFINING THE PARABOLIC SEGMENTS
45                    DO 10 I=1,N
                      C1(M,I)=Y(I)+Y)
                      C2(M,I)=(Y(I+1)-Y(I))/(X(I+1)-X(I))
                      C3(M,I)=-4.*DY(I)/(X(I+1)-X(I))**2
                   10 PRINT 3000,M,I,C1(M,I),C2(M,I),C3(M,I)
50               3000 FORMAT(1X,15HM,I,I,C1,C2,C3 =,2I5,1P3E12.4)
                      WHM)=C2(M,1)
                      RETURN
                C
                C COMPUTE J2E CORRESPONDING TO I2P
55              C
```

FIGURE C.3 LISTING OF SUBROUTINE J212P

```
      SUBROUTINE  J212P                                  CDC 6700 FTN V3.0-355F OPT=1  79/06/29. 1
                    20 N=NPS(M)
                       DO 30 I=1,N
                       IF(I2P.GT.X(I+1)) GO TO 30
                       IN=I
     60                GO TO 40
                    30 CONTINUE
                       PRINT 4000,J,I2P,X(N+1)
                  4000 FORMAT(//11H * * * CELL,I3,7H, I2P =,1PE12.4,47H, HAS EXCEEDED THE
                     1 LAST PRESCRIBED DATA POINT =,E12.4/7X,25HSOLUTION TERMINATED * *
     65                2*)
                       CALL EXIT
                    C
                    40 J2E=C1(M,IN)+(C2(M,IN)+C3(M,IN)*(I2P-X(IN+1)))*(I2P-X(IN))
                       IF(CBUG.EQ.1) PRINT 5000,IN,I2P,J2E
     70             5000 FORMAT(1X,13H IN,I2P,J2E =,I5,1P2E12.4)
                       RETURN
                       END
```

FIGURE C.3 LISTING OF SUBROUTINE J212P (Concluded)

DISTRIBUTION LIST

DEPARTMENT OF DEFENSE

Assistant to the Secretary of Defense
Atomic Energy
ATTN: Executive Assistant

Defense Advanced Rsch Proj Agency
ATTN: TIO
ATTN: G. Bulin

Defense Intelligence Agency
ATTN: DB-4N
ATTN: DB-4C, E. O'Farrell

Defense Nuclear Agency
2 cy ATTN: SPSS
4 cy ATTN: TITL

Defense Technical Information Center
12 cy ATTN: DD

Field Command
Defense Nuclear Agency
ATTN: FCPR
ATTN: FCTMOF

Field Command
Defense Nuclear Agency
Livermore Division
ATTN: FCPRL

Interservice Nuclear Weapons School
ATTN: TTV

Joint Strat Tgt Planning Staff
ATTN: NRI-STINFO Library
ATTN: JLA

NATO School (SHAPE)
ATTN: U.S. Documents Officer

Undersecretary of Def for Rsch & Engrg
ATTN: Strategic & Space Systems (OS)

DEPARTMENT OF THE ARMY

BMD Advanced Technology Center
Department of the Army
ATTN: ICRDABH-X
ATTN: ATC-T

Chief of Engineers
Department of the Army
ATTN: DAEN-MCE-D
ATTN: DAEN-RDM

Harry Diamond Laboratories
Department of the Army
ATTN: DELHD-N-P
ATTN: DELHD-I-TL

U.S. Army Ballistic Research Labs
ATTN: DRDAR-BLV
ATTN: DRDAR-TSB-S
ATTN: DRDAR-BLE, J. Keefer

DEPARTMENT OF THE ARMY (Continued)

U.S. Army Concepts Analysis Agency
ATTN: CSSA-ADL

U.S. Army Engineer Center
ATTN: DT-LRC

U.S. Army Engineer Div Huntsville
ATTN: HNDED-SR

U.S. Army Engineer Div Ohio River
ATTN: ORDAS-L

U.S. Army Engr Waterways Exper Station
ATTN: J. Strange
ATTN: WESSA, W. Flathau
ATTN: J. Zelasko
ATTN: WESSE, L. Ingram
ATTN: Library
ATTN: J. Drake
2 cy ATTN: WESSD, J. Jackson

U.S. Army Material & Mechanics Rsch Ctr
ATTN: Technical Library

U.S. Army Materiel Dev & Readiness Cmd
ATTN: DRXAM-TL

U.S. Army Missile R&D Command
ATTN: RSIC

U.S. Army Nuclear & Chemical Agency
ATTN: Library

DEPARTMENT OF THE NAVY

Naval Construction Battalion Center
ATTN: Code L08A
ATTN: Code L51, R. Odello
ATTN: Code L51, S. Takahashi

Naval Electronic Systems Command
ATTN: PME 117-21

Naval Material Command
ATTN: MAT 08T-22

Naval Postgraduate School
ATTN: Code 0142 Library
ATTN: G. Lindsay

Naval Research Laboratory
ATTN: Code 2627

Naval Surface Weapons Center
ATTN: Code F31

Naval Surface Weapons Center
ATTN: Tech Library & Info Services Branch

Naval War College
ATTN: Code E-11

DEPARTMENT OF THE NAVY (Continued)

Naval Weapons Evaluation Facility
ATTN: Code 10

Newport Laboratory
Naval Underwater Systems Center
ATTN: Code EM, J. Kalinowski

Office of Naval Research
ATTN: Code 715
ATTN: Code 474, N. Perrone

Office of the Chief of Naval Operations
ATTN: OP 981
ATTN: OP 03EG

Strategic Systems Project Office
Department of the Navy
ATTN: NSP-43

DEPARTMENT OF THE AIR FORCE

Air Force Geophysics Laboratory
ATTN: LWW, K. Thompson

Air Force Institute of Technology
ATTN: Library

Air Force Office of Scientific Research
ATTN: J. Allen
ATTN: W. Best

Headquarters
Air Force Systems Command
ATTN: DLW

Air Force Weapons Laboratory
Air Force Systems Command
ATTN: NTE, M. Plamondon
ATTN: NTES, R. Jolley
ATTN: NTES, J. Thomas
ATTN: NTES-C, R. Henny
ATTN: SUL

Assistant Chief of Staff, Intelligence
Department of the Air Force
ATTN: INT

Ballistic Missile Office
Air Force Systems Command
ATTN: MNNXH, D. Gage
ATTN: MNN
ATTN: MNNXH, M. Delvecchio

Research, Development, & Acq
Department of the Air Force
ATTN: AFRDQSM

Logistics & Engineering
Department of the Air Force
ATTN: LEEE

Foreign Technology Division
Air Force Systems Command
ATTN: NIIS Library

Rome Air Development Center
Air Force Systems Command
ATTN: TSLD

DEPARTMENT OF THE AIR FORCE (Continued)

Strategic Air Command
Department of the Air Force
ATTN: NRI-STINFO Library

Vela Seismology Center
ATTN: G. Ullrich

DEPARTMENT OF ENERGY

Department of Energy
Albuquerque Operations Office
ATTN: CTID

Department of Energy
Nevada Operations Office
ATTN: Mail & Records for Technical Library

OTHER GOVERNMENT AGENCIES

Central Intelligence Agency
ATTN: OSWR/NED

Department of the Interior
Bureau of Mines
ATTN: Technical Library

Federal Emergency Management Agency
ATTN: Hazard Eval & Vul Red Div

DEPARTMENT OF ENERGY CONTRACTORS

Lawrence Livermore National Laboratory
ATTN: L-96, L. Woodruff
ATTN: Technical Information Dept. Library

Los Alamos National Scientific Laboratory
ATTN: MS 364
ATTN: R. Bridwell
ATTN: MS 670, J. Hopkins

Oak Ridge National Laboratory
ATTN: Civil Def Res Proj
ATTN: Central Research Library

Sandia National Laboratories
Livermore Laboratory
ATTN: Library & Security Classification Div.

Sandia National Laboratories
ATTN: 3141
ATTN: A. Chabai
ATTN: L. Hill

DEPARTMENT OF DEFENSE CONTRACTORS

Aerospace Corp.
ATTN: Technical Information Services

Agbabian Associates
ATTN: M. Agbabian

Applied Theory, Inc.
2 cy ATTN: J. Trulio

AVCO Research & Systems Group
ATTN: Library A830

DEPARTMENT OF DEFENSE CONTRACTORS (Continued)

BDM Corp.
ATTN: T. Neighbors
ATTN: Corporate Library

Boeing Co.
ATTN: Aerospace Library

California Institute of Technology
ATTN: T. Ahrens

California Research & Technology, Inc.
ATTN: M. Rosenblatt
ATTN: S. Schuster
ATTN: Library
ATTN: K. Kreyenhagen

California Research & Technology, Inc.
ATTN: D. Orphal

Calspan Corp.
ATTN: Library

Civil Systems Inc.
ATTN: G. Melzer

University of Denver
Colorado Seminary
Denver Research Institute
ATTN: Sec Officer for J. Wisotski

EG&G Washington Analytical Services Center, Inc.
ATTN: Library

Eric H. Wang
Civil Engineering Rsch Fac
University of New Mexico
ATTN: N. Baum

Gard, Inc.
ATTN: G. Neidhardt

General Electric Company-TEMPO
ATTN: DASIAC

Higgins, Auld & Associates, Inc.
ATTN: N. Higgins
ATTN: H. Auld
ATTN: J. Bratton

Higgins, Auld & Associates, Inc.
ATTN: S. Blouin

IIT Research Institute
ATTN: Documents Library
ATTN: M. Johnson
ATTN: R. Welch

Institute for Defense Analyses
ATTN: Classified Library

J. H. Wiggins Co., Inc.
ATTN: J. Collins

Kaman AviDyne
ATTN: N. Hobbs
ATTN: Library

DEPARTMENT OF DEFENSE CONTRACTORS (Continued)

Kaman Sciences Corp.
ATTN: Library

Lockheed Missiles & Space Co., Inc.
ATTN: T. Geers
ATTN: Technical Information Center

Lovelace Biomedical & Environmental Research Institute, Inc.
ATTN: R. Jones

McDonnell Douglas Corp.
ATTN: R. Halprin

Merritt CASES, Inc.
ATTN: J. Merritt
ATTN: Library

Nathan M. Newmark Consult Eng Svcs
University of Illinois
ATTN: N. Newmark

Physics International Co.
ATTN: Technical Library
ATTN: E. Moore
ATTN: L. Behrmann
ATTN: F. Sauer
ATTN: J. Thomsen

R & D Associates
ATTN: J. Lewis
ATTN: J. Carpenter
ATTN: W. Wright, Jr.
ATTN: R. Port
ATTN: C. MacDonald
ATTN: Technical Information Center
ATTN: P. Haas

Science Applications, Inc.
ATTN: Technical Library

Science Applications, Inc.
ATTN: D. Maxwell
ATTN: D. Bernstein

Science Applications, Inc.
ATTN: W. Layson

Southwest Research Institute
ATTN: W. Baker
ATTN: A. Wenzel

SRI International
ATTN: T. Gupta
ATTN: G. Abrahamson
ATTN: B. Gaston
ATTN: D. Keough

Systems, Science & Software, Inc.
ATTN: T. Riney
ATTN: D. Grine
ATTN: Library
ATTN: T. Cherry

Systems, Science & Software, Inc.
ATTN: J. Murphy

DEPARTMENT OF DEFENSE CONTRACTORS (Continued)

Terra Tek, Inc.
ATTN: S. Green
ATTN: A. Abou-Sayed
ATTN: Library

Tetra Tech, Inc.
ATTN: L. Hwang
ATTN: Library

TRW Defense & Space Sys Group
ATTN: P. Bhutta
ATTN: Technical Information Center
2 cy ATTN: N. Lipner

TRW Defense & Space Sys Group
ATTN: P. Dai
ATTN: E. Wong

DEPARTMENT OF DEFENSE CONTRACTORS (Continued)

Universal Analytics, Inc.
ATTN: E. Field

Weidlinger Assoc., Consulting Engineers
ATTN: M. Baron

Weidlinger Assoc., Consulting Engineers
ATTN: J. Isenberg

Westinghouse Electric Corp.
ATTN: W. Volz